UNIVERSITY OF CRETE

SCHOOL OF HEALTH SCIENCES

DEPARTMENT OF BIOCHEMISTRY AND BIOTECHNOLOGY

INTERISTITUTIONAL PROGRAM OF POSTGRADUATE STUDIES

IN

ONCOLOGY

NATIONAL HELLENIC RESEARCH FOUNDATION

INSTITUTE OF CHEMICAL BIOLOGY

Ογκολογία

ΑΠΟ ΤΗΝ ΟΓΚΟΓΕΝΕΣΗ ΕΩΣ ΤΗ ΘΕΡΑΠΕΙΑ

MASTER THESIS

Photo- and Acid-Degradable Polyacylhydrazone–Doxorubicin Conjugates for controlled anticancer drug delivery

Σύνθεση και χαρακτηρισμός συζευγμένων πολυακυλο-υδραζονών - δοξορουβικίνης, διασπώμενων με φως και pH για την ελεγχόμενη απελευθέρωση αντικαρκινικών φαρμάκων

SUPERVISOR: Dr. Kyriakos Prousis, Associate Researcher, Institute of Chemical Biology, National Hellenic Research Foundation

KOTHRI MARTHA GEORGIA

A.M. 1140013

Heraklion, 18-10-2021

Η παρούσα διπλωματική εργασία εκπονήθηκε στο πλαίσιο σπουδών για την απόκτηση του Μεταπτυχιακού Διπλώματος Ειδίκευσης που απονέμει το Τμήμα Ιατρικής του Πανεπιστημίου Κρήτης, σε συνεργασία με το Ινστιτούτο Χημικής Βιολογίας του Εθνικού Ιδρύματος Ερευνών.

Εγκρίθηκε από τη κάτωθι τριμελή εξεταστική επιτροπή:

ΤΡΙΜΕΛΗΣ ΕΠΙΤΡΟΠΗ

ΟΝΟΜΑΤΕΠΩΝΥΜΟ	**ΒΑΘΜΙΔΑ**
Δρ. Κυριάκος Προυσής	Εντεταλμένος Ερευνητής, Συνθετική Φαρμακευτική Χημεία Βιοδραστικών στοχευμένων μορίων, ΙΧΒ | ΕΙΕ
Μαρία Βαμβακάκη	Καθηγήτρια, Τμήμα Επιστήμης και Τεχνολογίας Υλικών, Π.Κ
Δρ. Θεοδώρα Καλογεροπούλου	Διευθύντρια Ερευνών, Φαρμακευτική Χημεία, ΙΧΒ | ΕΙΕ

Acknowledgements

I would really like to thank everyone who has supported me and assisted in the fulfillment of my master thesis over the last two years.

First, I would like to thank Dr. Kyriakos Prousis, for his willingness to supervise this thesis and also Dr. Theodora Kalogeropoulou for participating in my committee. Foremost, I would like to express my sincere gratitude to my Professor Maria Vamvakaki for the continuous support of my master study and research, for her patience, motivation, and immense knowledge. Her guidance helped me in all the time of research and writing of this thesis.

My great appreciation also goes to PhD candidate Maria Psarrou for the collaboration, for her guidance and for all these things that I have learned from her in the lab through these years.

I want to thank my colleagues at the Synthetic Materials Chemistry lab, Dr. Maria Kaliva, Dr. Eva Vasilaki, Dr. Thodoris Manouras, Dimitra, Nikos, Stella, Dimitris G., Maria, Ioanna, Vasilis and Dimitris F. for their support and their collaboration.

Finally, the biggest appreciation goes to my parents and brother and of course, my beloved friends outside the lab and George, for their support and understanding my ‘’no time’’.

Στους γονείς μου,

Table of Contents

Abstract

Cancer is the second leading cause of death worldwide for both men and women and attacks even the very young ages. In the recent years, significant progress has been made on the development of pharmaceuticals for the treatment of cancerous tumors. However, the significant side effects of their conventional route of administration, i.e., the non-selective and uncontrolled delivery to cancer tissues, have driven the need for controlled drug delivery systems. Drug delivery systems can safely deliver a drug substance by combining a suitable material with bioactive molecules or drugs that would otherwise have inadequate activity or undesirable pharmacokinetic characteristics or would be toxic to healthy normal cells. Polymeric drug delivery systems that have been investigated range from polymeric micelles, vesicles, hydrogels, etc. The aim of this thesis is to report the synthesis and characterization of a new, linear, main-chain photo- and acid-degradable copolymer based on acylhydrazone linkages. The polymer synthesis was carried out by the step-growth copolymerization of adipic acid dihydrazide with a bifunctional poly (ethylene glycol) bearing benzaldehyde end-groups, under mild acidic conditions, to afford hydrophilic PEG-*alt*-adipic acid (PEG-*alt*-AA) alternating copolymers. The synthesized polymers were characterized by size exclusion chromatography, proton nuclear magnetic resonance and attenuated total reflection-Fourier transform infrared spectroscopies. The main-chain photo- and acid-induced degradation of the copolymers in dimethylsulfoxide and water, respectively, to produce the two precursor comonomers, was verified by UV-vis spectroscopy at light intensities as low as 0.1 mW cm^{-2} at λ = 254 nm. Next, a model anticancer drug, doxorubicin (DOX), was chemically linked to the polymer chain end(s) via acylhydrazone bond(s), resulting in amphiphilic PEG-*alt*-adipic acid-DOX (PEG-*alt*-AA-DOX) polymer–drug conjugates. The conjugates were self-assembled in water to form spherical nanoparticles, as evidenced by scanning and transmission electron microscopies and dynamic light scattering. The irradiation of the self-assembled PEG-*alt*-AA-DOX conjugates with UV light and the simultaneous decrease of the solution pH resulted in the disruption of the assemblies, due to the combined photolysis and acidolysis of the acylhydrazone bonds, and led to the controlled release of the therapeutic cargo.

Keywords: cancer, drug delivery systems, polyacylhydrazones, photo- and acid-degradable polymers, polymer-drug conjugates, doxorubicin, control release

Περίληψη

Ο καρκίνος αποτελεί τη δεύτερη, κύρια αιτία θανάτου παγκοσμίως, τόσο για άνδρες όσο και για γυναίκες, προσβάλλοντας ακόμη και πολύ μικρές ηλικίες. Τα τελευταία χρόνια έχει επιτευχθεί σημαντική πρόοδος στην ανάπτυξη φαρμακευτικών ουσιών για την αντιμετώπιση των καρκινικών όγκων. Ωστόσο, οι σημαντικές παρενέργειες που παρουσιάζονται από το συμβατικό τρόπο χορήγησης τους, εξαιτίας της μη εκλεκτικότητάς τους και μη ελεγχόμενης διάθεσής τους στους καρκινικούς ιστούς, έχουν οδηγήσει στην εισαγωγή τους σε συστήματα ελεγχόμενης χορήγησης. Τα συστήματα μεταφοράς φαρμάκων έχουν την ικανότητα της ασφαλούς μεταφοράς μιας φαρμακευτικής ουσίας συνδυάζοντας υλικά με βιο-ενεργά μόρια ή φάρμακα τα οποία σε διαφορετική περίπτωση θα είχαν ανεπαρκή ή μη επιθυμητά φαρμακοκινητικά χαρακτηριστικά ή θα ήταν τοξικά για τα υγιή φυσιολογικά κύτταρα. Τα πολυμερικά συστήματα μεταφοράς φαρμάκων περιέχουν ένα εύρος μακρομοριακών δομών που κυμαίνονται από πολυμερικά μικκύλια μέχρι σύνθετα συστήματα είτε με μακρομόρια είτε με πρωτεΐνες. Στόχος της παρούσας διπλωματικής εργασίας, είναι η σύνθεση και ο χαρακτηρισμός ενός νέου συζευγμένου συστήματος πολυμερούς – φαρμάκου, που μπορεί να διασπαστεί με φως και pH, εξαιτίας των δεσμών ακυλο-υδραζόνης που περιέχει, για την ελεγχόμενη απελευθέρωση του αντικαρκινικού φαρμάκου. Η σύνθεση της πολυμερικής αλυσίδας πραγματοποιήθηκε μέσω πολυμερισμού πολυσυμπύκνωσης της διυδραζίνης του αδιπικού οξέος, με μια διδραστική πολύ(αιθυλενογλυκόλη) που φέρει τελικές ομάδες βενζαλδεΰδης (PEG_{ald}), υπό ήπια όξινες συνθήκες, για την παραγωγή ενός υδρόφιλου εναλλασσόμενου συμπολυμεριμερούς, PEG-alt-αδιπικό οξύ (PEG-alt-AA). Τα συντιθέμενα πολυμερή χαρακτηρίστηκαν με χρωματογραφία αποκλεισμού μεγεθών και φασματοσκοπίες πυρηνικού μαγνητικού συντονισμού πρωτονίου και υπερύθρου με μετασχηματισμό Fourier, αποσβένουσας ολικής ανάκλασης. Η διάσπαση της πολυμερικής αλυσίδας σε διμεθυλοσουλφοξείδιο και νερό, υπό την επίδραση του φωτός (UV ακτινοβολίας σε λ=254nm και χαμηλή ένταση 0.1 mW cm^{-2}) και όξινου pH αντίστοιχα, επαληθεύτηκε με φασματοσκοπία υπεριώδους-ορατού. Στη συνέχεια, ένα πρότυπο αντικαρκινικό φάρμακο, η δοξορουβικίνη (DOX), προσδέθηκε χημικά στο(α) άκρο(α) της αλυσίδας του πολυμερούς, μέσω δεσμών ακυλοϋδραζόνης, για τη σύνθεση του αμφίφιλου συζευγμένου συστήματος πολυμερούς – φαρμάκου, PEG-alt-αδιπικό οξύ-DOX (PEG-alt-AA-DOX). Αυτά τα συζευγμένα συστήματα, εξαιτίας του αμφίφιλου χαρακτήρα τους, αυτοοργανώθηκαν σε νερό για τον σχηματισμό σφαιρικών νανοσωματιδίων, όπως αποδεικνύεται από τις μικροσκοπίες ηλεκτρονικής σάρωσης και μετάδοσης και τη μέτρηση δυναμικής σκέδασης φωτός. Η ακτινοβόληση, τέλος, των αυτοοργανωμένων συζευγμένων συστημάτων PEG-alt-AA-DOX με υπεριώδη ακτινοβολία και η

ταυτόχρονη μείωση του pH του διαλύματος είχε ως αποτέλεσμα τη διάσπαση των νανοσωματιδίων, λόγω της συνδυασμένης φωτόλυσης και όξινης υδρόλυσης των δεσμών ακυλοϋδραζόνης που οδήγησε στην ελεγχόμενη αποδέσμευση του θεραπευτικού φορτίου.

Λέξεις κλειδιά: καρκίνος, συστήματα μεταφοράς φαρμάκων, πολυακυλοϋδραζόνες, πολυμερή που διασπώνται με φως και όξινο pH, συζευγμένα συστήματα πολυμερών φαρμάκων, δοξορουβικίνη, ελεγχόμενη απελευθέρωση.

Chapter 1

Introduction

1.1 Cancer

Cancer is a prominent cause of death and a significant impediment to extending life expectancy in every country. According to the World Health Organization (WHO), cancer was the first or second leading cause of death before the age of 70 in 112 of 183 countries in 2019, and third or fourth in another 23 countries. Cancer's rising prominence as a leading cause of death partly reflects marked declines in mortality rates of stroke and coronary heart disease, relative to cancer, in many countries [1]. There were an estimated 19.3 million new cases of cancer and almost 10.0 million deaths from cancer worldwide in 2020. The most commonly diagnosed cancers worldwide were female breast cancer (2.26 million cases), lung (2.21 million cases) and prostate cancers (1.41million cases) and as for the most common causes of cancer death, these were lung (1.79 million deaths), liver (830,000 deaths) and stomach cancers (769,000 deaths) [2].

Cancer is a genetic disease that arises when the information in cellular DNA is corrupted leading to abnormal patterns of gene expression. As a result, the effects of normal genes that control cell growth, survival and spread are augmented while genes that suppress these effects are repressed. The accumulation of mutations is the main mechanism by which this corruption of the genetic code occurs, although there is an increasing awareness of the involvement of non-mutational (epigenetic) alterations in the process [3]. Cancer cells are defined by two inherited properties: (1) they reproduce defying physiological constraints on their development and division cells and (2) invade areas normally intended for others cells. The combination of these characteristics is what makes cancer particularly dangerous. An abnormal cell that grows, increasing its mass and its uncontrolled proliferation will lead to a tumor. As far as tumor cells do not penetrate into the surrounding tissues, the tumor is considered as benign, and the removal or destruction of the mass locally usually leads to a successful cure. A tumor is considered cancerous only if it is malignant, that is, only if its cells have acquired the ability to invade the surrounding tissue. Penetration is an essential characteristic of cancer cells. It allows their vascularization through the circulatory system and thus their spread to other areas of the body, forming secondary tumors called metastases. The wider is the spread of a cancer, the more difficult it is to eradicate it and metastases are generally what kill the cancer patient [4].

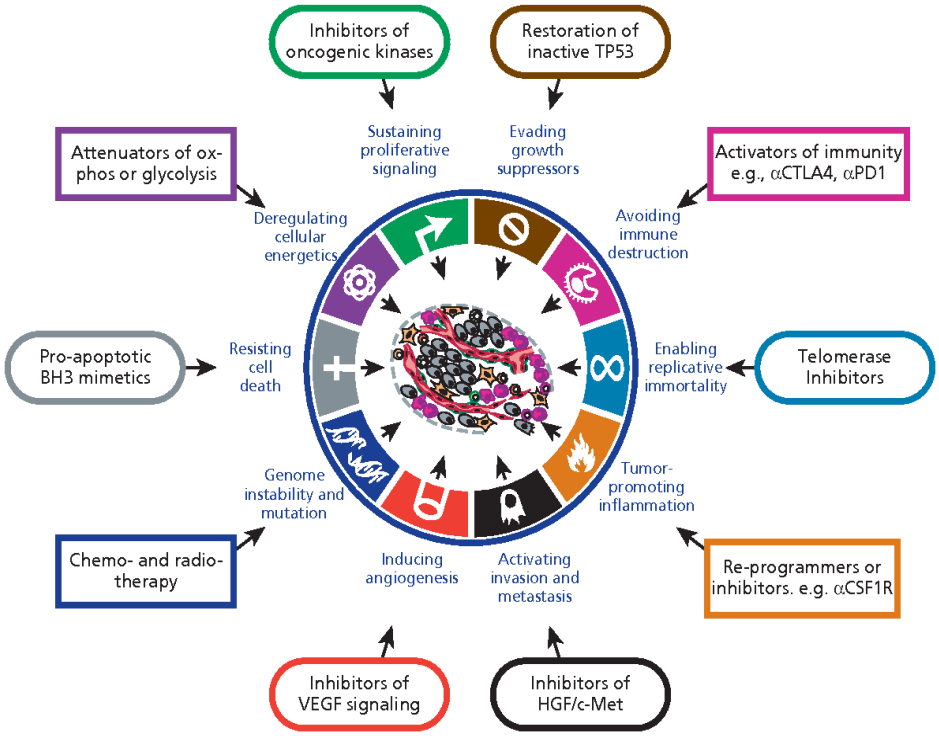

Figure 1.1. Hallmarks of Cancer and their therapeutic targeting.

Since the introduction of the six cancer features in 2000 by Hanahan and Weinberg, great progress has been made in understanding and treating the disease. As shown in **Figure 1.1**, cancer cells have some characteristics that allow tumor growth and metastasis. The abnormal growth of the tumor is the result of many mutations that affect cell growth, differentiation, survival and death. Although, these mutations vary from one neoplastic disease to another, cancer cells have some distinct features, which are similar in most types of cancer. The characteristics of cancer, as established by Hanahan and Weinberg in 2011 are [5]:

1. Resistance to the mechanisms of programmed cell death and apoptosis avoidance
2. Self-sufficiency in growth signals
3. Suppression of anti-growth signals
4. Genetic instability and mutations
5. Continuous angiogenesis
6. Invasion and metastasis
7. Inflammation that promotes cancer

8. Deregulation of cellular metabolism

9. Avoid immuno-destruction

10. Uncontrolled proliferation

1.2 Cancer Therapy and Anti-cancer Drugs

Although cancer treatment options have both increased in quantity and improved in quality recently, there is still much work to be done to improve overall cancer survivability and quality of life, while patients undergo cancer treatment. All of the above, highlight the urgency and priority that is currently placed on translatable cancer research. Despite countless advances in cancer medicine, cancer treatment is still a huge challenge for researchers, health care providers, and patients alike. Unlike treating a microbial infection, where a discrete invader or unruly cohabitant is the source of illness, cancer poses the unique challenge of being almost indistinguishable from the rest of the organism. Cancer cells are a diseased version of the self, making their isolation and treatment extraordinarily difficult. Thus, cancer treatment depends on very subtle differences between the healthy cells and cancer cells (in comparison to the large differences between prokaryotic cells and eukaryotic cells in a bacterial infection, for example).

Several approaches have been used in cancer treatment, including surgery, radiation therapy, chemotherapy, immunotherapy, targeted therapy, hormone therapy and stem cell transplant.

1.2.1 Chemotherapy: Advantages and Disadvantages

Attempts to treat cancer with chemical entities date back in 1800 BC, when preparations of plant and herbal medicines were used. Over the years it has been repeatedly shown that natural products isolated from a range of sources can have highly potent anti-tumor activities. However, the concept of chemotherapy was first introduced by Paul Ehrlich, a German physician and scientist. Ehrlich pioneered the use of dyes for histological studies and bacterial diagnostics, and this work led him to identify agents which could bind to specific cellular components [6]. In 1908, he was awarded the Nobel Prize in Physiology and Medicine because of his theory of the immune system and the discovery of antibodies behaving in a highly specific manner in response to infection [7].

One of the main aims in the development of new chemotherapies is to be selective against proliferating tumor cells over non-proliferating normal healthy cells. Many commonly used anti-cancer drugs are more effective against tissues with a higher portion of dividing cells, the proportion which is often called ‘growth fraction’. Since it is the dividing cells that are targeted by chemotherapeutic drugs, it has been observed that cancer cells and normal tissues with high growth fractions are more susceptible to be affected by anti-cancer drugs.

However, when the cancer cells are killed by a good and efficient chemotherapy, normal tissues with a high growth fraction, such as bone marrow, hair follicles and gastrointestinal mucosa, are also damaged by anti-cancer drugs, leading to significant adverse effects. For example, damage of bone marrow, bleeding and infection are some examples of complications of cancer treatment. Thus, the aim of chemotherapy is to enhance the toxicity specifically targeted to cancer cells, while at the same time reducing the side effects on normal cells. Advances in the development of cancer treatments has led to more anti-cancer agents for use in tumor therapy such as proteins, oligo-peptides, antibodies, hormones, nucleic acids, growth factors and others. The major problem with chemotherapy in the treatment of cancer is its lack of selectivity when destroying cancer or normal cells. The efficacy of cancer chemotherapy is limited by the poor uptake of the drugs by cancerous cells and the high toxicity to normal cells. In addition, most of the anti-cancer drugs are water-insoluble and thus have poor cellular uptake.

1.2.2 Drug Delivery Systems

In order to overcome the drawbacks of conventional chemotherapy, an increased interest has been focused on nanotechnological approaches in cancer treatment, based on the concept that pharmacokinetics of an anticancer drug can be altered in the body to promote drug accumulation predominantly at pathological sites [8]. Such a strategy is aimed to improve the treatment ability to target and kill cells of diseased tissues/organs, while affecting as few healthy cells as possible. Several reviews, have focused on the potential of nanotechnology in cancer therapy and have discussed how different nanoparticulate drug-delivery systems perform in this field [9, 10]. The therapeutic effects of many anticancer drugs could be significantly improved if the delivery of the drug occurs specifically to tumors (cancer cells) or preferably inside specific organelles of the cells and reduction of the toxic side effects of the drug is achieved. In this respect, a multifunctional construct based on novel nanomaterials can be delivered directly to the tumor site and eradicate cancer cells selectively. An appropriate design allows these nanoconstructures to improve drug

efficacy (activity at lower doses) as compared to the free-drug treatment, which in turn gives a wider therapeutic window and lower side effects. Furthermore, nanocarriers are also capable of addressing several drug delivery problems, which could not be effectively solved in the past, like penetrating cellular barriers that may limit device accessibility to intended targets, such as the blood–brain barrier, among others.

Table 1.1. Advantages of Drug Delivery Systems for cancer treatment

1. Increase the concentration of the medication in the sick area, while lowering its concentration in healthy tissues.
2. Reduce toxicity and adverse effects
3. Increase the solubility of drugs
4. Improve drug stability and decrease drug breakdown during circulation
5. Reduce the amount of doses to make the patient's experience less unpleasant.
6. Multiple medicines can be delivered at the same time to particular locations to improve treatment.
7. Drugs and screening agent co-delivery

1.2.3 Tumor Targeting

In principle, delivery of anticancer drugs to tumor tissues can be achieved by either passive or active targeting (**Figure 1.2**).

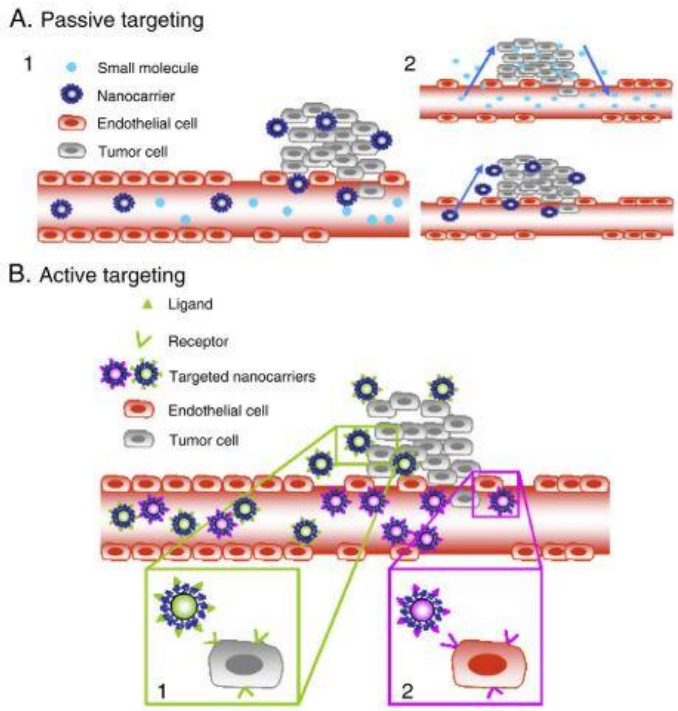

Figure 1.2. A. Passive targeting of nanocarriers. (1) Nanocarriers reach tumors through the leaky vasculature surrounding the tumors. (2) Representation of the influence of the size for retention in the tumor tissue. Small molecules diffuse freely in and out the tumor blood vessels because of their small size. By contrast, drug-loaded nanocarriers cannot diffuse back into the blood stream because of their large size, resulting in progressive accumulation: the EPR effect. B. Active tumor targeting of (1) cancer cells or (2) angiogenic endothelial cells by specific ligands at the surface of the nanocarriers [11].

1.2.3.1 Passive targeting: Enhanced Permeability and Retention (EPR) effect

The accumulation of a drug or a drug carrier system at a desired site owing to physicochemical or physiological factors is referred as passive targeting. It takes advantage of the size of the nanocarriers and the unique properties of the tumor vasculature and microenvironment.

For further growth and enlargement, tumors need to form new blood vessels, via the angiogenesis process, in order to obtain nutrients and sustain their growth. Tumor vessels are generally abnormal and have aberrant branching, blind loops of twisted form, which are characterized by architectural defeciency and a high degree of vascular density. The newly formed tumor blood vessels usually present an abnormal architecture too, including defective endothelial cells with wide fenestrations, irregular vascular alignment, lack of a smooth muscle layer or innervation and

wide lumen. Blood flow behavior, such as direction of blood flow, is also irregular or inconsistent in these vessels. Tumor vessels are “leaky” when compared with normal vessels, owing to basement membrane abnormalities and a reduced number of pericytes lining the rapidly proliferating endothelial cells. Indeed, the pore size of tumor vessels varies from 100 nm to almost 1 mm in diameter, depending upon the anatomic location of the tumors and the stage of tumor growth. In comparison, the tight endothelial junctions of normal vessels are typically of 5-10 nm in size. The leaky and defective architecture of tumor vasculature might be due to elevated levels of vascular mediators such as bradykinins, nitric oxide, VEGF, basic fibroblast growth factor, prostaglandins and so on. Moreover, solid tumors are also characterized by the lack of a lymphatic network that decreases the clearance of macromolecules giving, consequently, extended retention times in the tumor interstitial fluid [12]. The unique pathophysiologic characteristics of tumor vessels coupled with their poor lymphatic drainage (**Figure 1.3**) induces the EPR effect, which enables macromolecules, including nanocarriers, to extravasate through these gaps into extravascular spaces and accumulate inside tumor tissues.

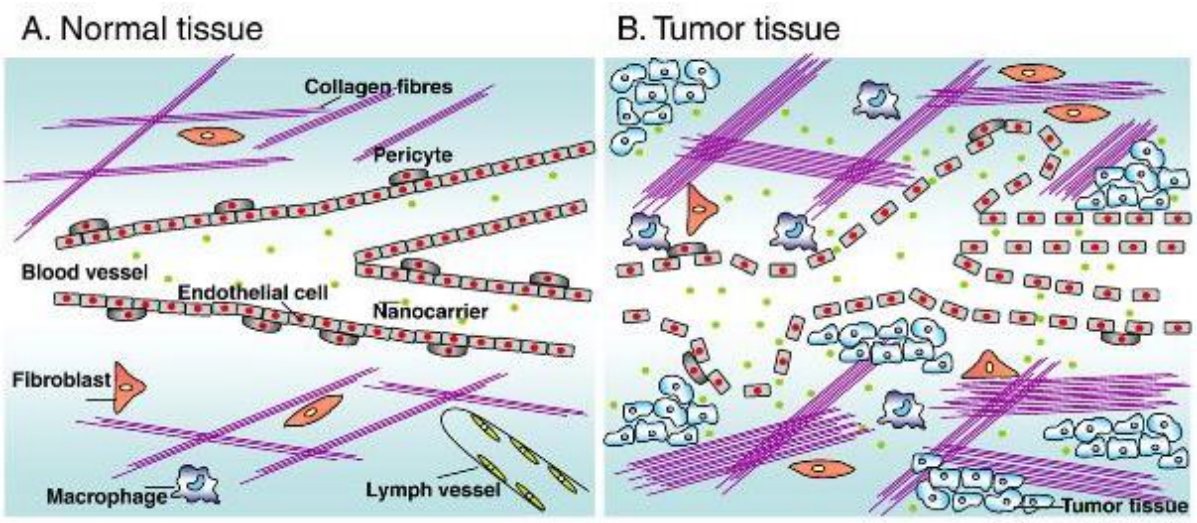

Figure 1.3. Differences between normal and tumor tissues that explain the passive targeting of nanocarriers by the EPR. **A.** Normal tissues contain linear blood vessels maintained by pericytes. Collagen fibers, fibroblasts and macrophages are in the extracellular matrix. Lymph vessels are present. **B.** Tumor tissues contain defective blood vessels with many sac-like formations and fenestrations. The extracellular matrix contains more collagen fibers, fibroblasts and macrophages than in normal tissue. Lymph vessels are lacking [11].

The EPR effect reported by Matsumura and Maeda in 1986 [13] was commented by Torchilin [14] as a molecular weight-dependent phenomenon: particles larger than 40 kDa, which is the threshold for renal clearance, show a prolonged circulation time (thus, a much increased half-life) and hence very slow clearance from the body. Thus, these molecules permeate gradually tumors in a selective fashion. However, targeting cancer cells using the EPR effect is not feasible in all tumors because the degree of tumor vascularization and porosity of tumor vessels can vary with the tumor type and status, according to recent studies [15, 16]. One approach to overcome this limitation is to attach targeting moieties to the nanocarrier surfaces, thus forming an “active nanocarrier”.

1.2.3.2 Active Tumor Targeting

Contrary to passive drug targeting, active drug targeting relies on the use on certain ligands (usually antibodies or peptides) that can be grafted covalently to the nanocarrier surface and specifically bind to overexpressed receptors at the target site (**Figure 1.2 B**) [17]. In active targeting, there are two cellular targets: (i) the targeting of cancer cells (overexpression of Epidermal Growth Factor Receptor (EGFR) or Glycoproteins receptors) and (ii) the targeting of the tumor endothelium (overexpression of the Vascular Endothelial Growth Factors (VEGF) for example). Because of the "binding-site barrier," the ligands' affinity for the receptor is critical for the penetration of the nanocarrier into the tumor [18]. The active targeting strategy promises to target the cancer tissue more specifically than with the EPR effect alone.

1.3. Classification of different types of Drug Delivery Systems

The gigantically expanding need for more compelling anticancer treatments has prompted, as already discussed, the plan and advancement of a few inventive drug delivery systems. In view of this earnest need, a wide scope of novel drug carriers have been developed for the controlled and efficient delivery of payloads to target sites. Regarding their composition and structure, nanocarrier platforms for cancer can be categorized as organic-based, inorganic-based or a hybrid combination of the aforementioned. Organic nanoplatforms include polymeric nanocarriers, lipid-based nanocarriers (e.g., liposomes and nanoemulsions), dendrimers, and carbon-based nanocarriers (e.g., fullerenes and carbon nanotubes). Metallic nanostructures, silica nanoparticles, and quantum dots are examples of inorganic nanoplatforms.

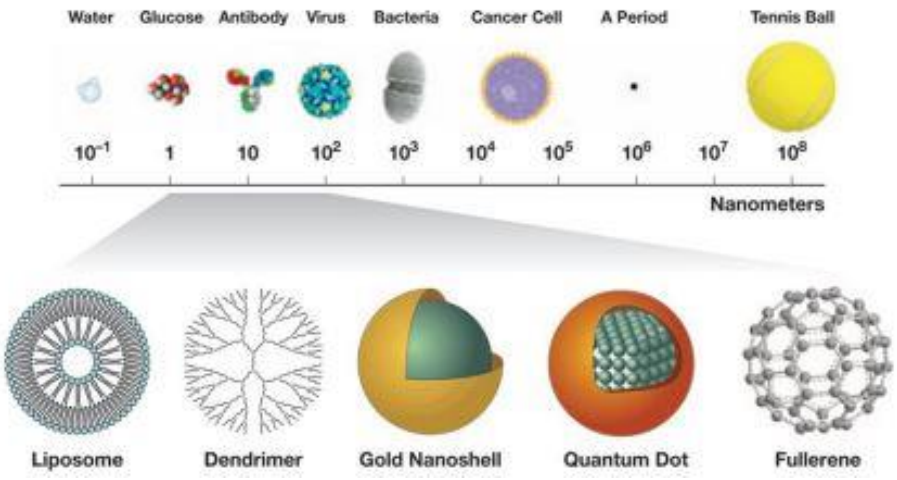

Figure 1.4. Nanometer scale comparison of nanocarriers to other materials [19].

1.3.1 Inorganic nanocarriers

In the recent years, inorganic materials have shown great potential as nanocarriers in drug delivery systems. There are various investigations on these materials showing the effective delivery of bioactive mixtures and their low side effects and toxicity to normal tissues [20, 21]. The most commonly used inorganic materials for such applications are quantum dots, silica nanoparticles, iron oxide, gold and magnetic nanoparticles. Among them, there are mainly two types consisting of iron- and gold-nanomaterials that have been clinically approved and/or are undergoing clinical trials for antitumor therapies. For example, for iron-based nanomaterials, which have exerted considerable impacts on therapeutics, in 2010, Nanotherm™ (aminosilane-coated superparamagnetic iron oxide nanoparticles) was approved by EMA for glioblastoma treatment via local hyperthermia [22]. After the nearby infusion of Nanotherm™ into tumors, the nanoparticles were heated by an alternating magnetic field applicator to achieve a higher local temperature of the tumor environment at 40−45 °C, resulting in programmed and nonprogrammed cell death. Another example of inorganic nanomaterials in preclinical trials, this time silica-gold nanoshells coated with PEG, AuroLase®, was developed for photothermal ablation of solid tumors with stimulation by NIR irradiation. Preclinical animal – level researches demonstrated that AuroLase® could be applied to induce photothermal cell death after activation by NIR irradiation in vitro and increase the tumor microenvironment temperatures to cause irreversible damage to solid tumors [23]. Although these results seem promising, there are still serious

concerns about their cytotoxicity (as most of them are not biocompatible), hydrophobicity and excretion pathway [24].

1.3.2 Organic nanocarriers

Organic nanocarriers can be synthetic or natural in origin. In contrary to inorganic nanocarriers, drug delivery systems consisting of organic materials have received more attention, because in most cases, they are based on biocompatible and biodegradable molecules. To prepare organic nanocarriers, small organic molecules self-assemble covalently and/or non-covalently to form three-dimensional structures such as liposomes, dendrimers and polymer – based nanocarriers (like polymeric micelles, polymersomes and polymeric conjugates). These interesting structures provide a suitable environment for the packaging and transport of bioactive molecules including anticancer drugs, genes, antibodies and a number of other lipophilic or hydrophilic molecules. Their promising behavior as future therapeutic agents has been studied for many years, and several of these organic nanocomposites have been introduced in the clinic [25, 26].

1.3.2.1 Liposomes

Liposomes are one of the oldest nanoparticulate drug carriers designed to improve drug pharmacokinetics and biodistribution [27]. Liposomes are composed of various lipids in a mono- or bi-layer forming a spherical vesicle surrounding an aqueous core. They can be designed to range greatly in size (from about 10 nm to over 1 μm) and in surface properties, like charge and functionality, using various combinations of commercially available lipids. Another benefit of the aqueous core surrounded by a layer of lipid structure is that both hydrophilic and hydrophobic drugs can be loaded in each compartment, respectively. However, liposomes suffer from a low encapsulation capacity, poor drug solubility, and instability in the bloodstream that leads to a very quick-burst release of the loaded drugs. Some of these shortcomings can be addressed with functionalized coatings, like polyethylene glycol (PEG), which increase the stability and circulation half-life of the liposomes [28]. However, even uncoated liposomes offer an improvement over the half-life of the free drug.

1.3.2.2 Dendrimers

Another type of drug delivery systems of interest are polymeric dendrimers. Dendrimers are super branched macromolecules with a tree-like structure. They present three different parts: a central hydrophobic core, ramification units called "Generations" and hydrophilic functional groups at the external side that can be conjugated with specific molecules for a targeting activity. They have attracted a lot of attention as drug carriers, due to their unique characteristics such as their well-defined size, shape and molecular weight, monodispersity and high degree of surface functionalities. The internal cavities of the dendritic structure provide a suitable environment for the entrapment or encapsulation of hydrophobic compounds, while functional groups on the surface can be used to deliver hydrophilic agents or genes [29].

1.3.2.3 Polymer micelles

Polymer micelles are macromolecular assemblies that are formed from AB type or ABA type amphiphilic block polymers. They have many advantages to support their biological applications, such as being biodegradable, non-toxic, biocompatible and non-immunogenic. Generally, polymer micelles are spherical nanostructures and consist of a hydrophobic inner core and a hydrophilic outer shell. The sizes of the polymer micelles range between 10 and 200 nm in diameter, which also categorize them as nanoparticulate drug delivery systems. Water-insoluble drugs can be encapsulated inside the hydrophobic core physically via self-assembly or chemically linked through covalent bonds. Due to the hydrophilicity of the outer shell and the biodegradability of the polymer micelle, this drug delivery system can maximize tissue compatibility, increase the half-life in plasma and minimize the cytotoxicity of the hydrophobic drug [30].

1.3.2.4 Polymersomes

Polymersomes are polymer-based vesicular shells that are formed upon hydration of amphiphilic block copolymers. Known as nanocapsules, polymersomes are indeed vesicular systems in which the drug is confined to a reservoir or within a cavity surrounded by a polymer coating. Accurate selection of the polymer, hydrophilic/hydrophobic ratio and chemistry impart polymersomes with a broad and tunable range of carrier properties. These systems are capable of encapsulating a large range of therapeutically water soluble active molecules and biomolecules [31].

1.4 Polymer – Drug Conjugates

Polymer therapeutics have been studied for over four decades and one of the most studied approaches for polymer therapies is polymer-drug conjugates. Polymer-drug conjugates (also known as polymeric prodrugs) are drug delivery systems in which one or more drugs are chemically attached to the functional groups of the polymer directly or through a spacer [32]. The spacer is usually a stimuli-sensitive linker, meaning that it undergoes dissociation under certain conditions. The concept of polymer–drug conjugates was first proposed in 1975 by Ringsdorf for the delivery of hydrophobic small molecular drugs to their site of action [33]. Further pioneering work by Duncan et al. focused on the design of a series of poly(N-(2-hydroxypropyl) methacrylamide) copolymer-anticancer drug conjugates [34]. From then on, conjugation of a drug to a biocompatible polymer has become one of the novel strategies for anticancer drug delivery. It is worth mentioning that polymer – drug conjugates are among the several types of nanocarriers that are currently in clinical trials as far as Phase III. For instance, poly(N-(2-hydroxypropyl) methacrylamide) copolymer (HPMA)-doxorubicin was the first synthetic polymer-anti-cancer drug conjugate to enter clinical trials about two decades ago [35]. With a few exceptions, water-soluble polymer–drug conjugates (polymer prodrugs) generally consist of (i) a water-soluble polymer backbone of variable architecture that provides the conjugate biocompatibility and good solubility, while ensuring its extended circulation in the body, (ii) a biologically active molecule, which is typically a low molecular weight drug, and (iii) a biodegradable linkage between the drug and the polymer chain. The major advantage of using polymer-drug conjugates is that the chemical and physical properties of polymers can be tuned to increase the efficacy and to reduce the toxicity of the drug. Besides that, the covalent attachment of the drug onto the polymer prevents the passive diffusion of the drug and its leakage from the carrier during blood circulation, which is a common problem in physically entrapped drugs within nanocarriers, resulting in a lower drug accumulation at the tissue of interest. Furthermore, the incorporation of stimuli-degradable drug-polymer linkages allow the site-specific drug release and increase its therapeutic efficacy [36, 37]. At last, another important characteristic is that amphiphilic polymer-drug conjugates in aqueous solution can form micelles or micelle-like nanoassemblies in which the lipophilic drug is confined in the internal core of the system giving the ability to protect the drug against premature metabolism in transit.

On the other hand, most of the clinical polymer–drug conjugates are not biodegradable. Their molecular masses are limited to several thousands to ensure renal elimination. As the polymer backbone is non-degradable, the polymer–drug linker is critical for drug release and needs a

special design to ensure cleavage at a pointed site and in a desired manner. Even though there are a few studies on stimuli-activatable prodrugs, polymer-drug conjugates based on a main-chain photodegradation mechanism have been scarcely reported in the literature [38].

1.4.1 Self-assembly of amphiphilic polymer-drug conjugates

Self-assembly refers to the process by which multiple components spontaneously organize to form a larger entity.[39] Molecular self-assembly is common in nature and in everyday life. The self-assembly of phospholipids forms the membranes of living cells. Soap bubbles, which are observed while using soaps, are produced by the self-assembly of tiny surfactant molecules. Self-assembly of molecules and subsequent formation of well-defined micro- and nanostructures has multiple interesting applications in nanosciences and nanotechnology. Such a mechanism relies on weak noncovalent bonds, such as hydrogen and ionic bonds, or van der Waals and hydrophobic interactions, and it can be applied to fabricate various complex micro- and nanostructures, such as flowers, tubes, rods, micelles, films, membranes, mesophases, particles, and hollow sphere structures (**Figure 1.5**). Amphiphiles are compounds possessing both hydrophilic (water-loving) and lipophilic (fat-loving) or water-hating components. The most common preparation methods for the self-assembly of amphiphilic macromolecules are the selective solvent method, the thin film hydration method and the selective-non selective solvent method. In amphiphilic macromolecules, the lipophilic segments become packed together, as it is more entropically favorable and create a hydrophobic environment, which is the core of the micelles. On the other hand, the hydrophilic parts are preferentially dissolved in water and create a flexible corona which is the outer shell of the micelles.

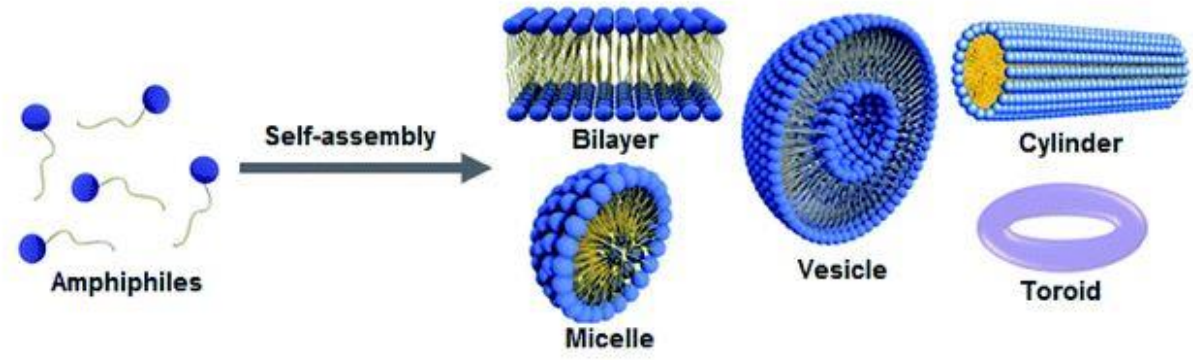

Figure 1.5. Amphiphiles self-assembled into various shapes such as bilayers, micelles, vesicles, cylinders and toroids [40].

Israellachvili et al. established a model-based theory that examines the geometry of individual molecules to clarify the morphology of the structures [41]. According to this theory, the nanostructure produced in aqueous solution by amphiphilic molucules may be determined by calculating the packing of the amphiphile as defined by the critical packing parameter (p).

$$p = v/a_0 l_c$$

Where v is the effective volume filled by the hydrophobic part in the core, a_0 is the equilibrium area of the hydrophilic surface group, and l_c is the individual amphiphile's maximum effective chain length. The aggregates, depending on the p value, can be micellar ($p \leq 1/3$), cylindrical ($1/3 \leq p \leq 1/2$), vesicular ($1/2 \leq p \leq 1$), or lamellar ($p = 1$). Since the packing parameter p is sometimes difficult to calculate the hydrophilic and hydrophobic mass fractions, which relate to the volume fractions, are more commonly considered. It is described in the literature that, upon increasing the relative block volume fractions of the hydrophobic domain to the hydrophilic domain, the self-assemblies would undergo a structural transition from micelles to worms to vesicles [42].

The key characteristic of self-assembling polymer-drug conjugates is that they are amphiphilic in nature, possessing both hydrophilic and hydrophobic domains that enable aqueous assembly — either spontaneously or via kinetic trapping (e.g. nanoprecipitation). The drug itself typically constitutes one of these two domains, most commonly the hydrophobic, with the polymer forming the other. As a result in addition to eliciting a therapeutic effect, the drug also performs a structural function. As both polar and non-polar regions coexist, the self-assembly of amphiphilic polymer-drug conjugates can be readily aided by thermodynamics. By self-assembling into well-defined nanostructures, the resultant assemblies have a distinct, typically enhanced, pharmacokinetic profile and may possess unique properties in tuning drug release rates and addressing multidrug resistance.

Kataoka and co-workers reported that, for extremely hydrophobic drugs, their attachment to a polymer often led to unwanted aggregation, or even precipitation [43]. Rather than viewing this as a limitation of the polymer-drug conjugates as drug delivery systems, they saw the potential opportunity to utilize the observed self-aggregation behavior to create micelles from the polymer-drug conjugates. In their early reports, the Kataoka group described the direct conjugation of multiple adriamycin (ADR) molecules to a poly(ethylene glycol)-poly(aspartic acid) block copolymer, to prepare PEG-*b*-P(Asp(ADR)). When dispersed in aqueous solution, these conjugates associated into spherical micelles with average diameters of 50 nm [44]. Since then, the development of self-assembling polymer-drug conjugates has grown to become an area of

considerable interest. Most of the reported literature focuses on the self-assembly of amphiphilic block copolymers, however conjugation to single component polymers, has been also investigated. For instance, Liu et al. conjugated docetaxel to a medium molecular weight PEG (Mw > 2 kDa), generating spherical micelles ~46 nm in diameter [45].

1.5 Stimuli Degradable Polymers

Stimuli-degradable or stimuli-sensitive polymers are described as polymers that undergo abrupt physiochemical changes or usually irreversible bond breakage, in response to small external changes in the environmental conditions. Stimuli-degradable polymers (SDPs) have gained increasing attention due of their wide range of potential application in various fields, including nano- and bio-technology as drug carriers, actuators, in bio-patterning, etc. [46]. The cleavable bonds can be located in the main-chain of a polymer or in the side chain. In both cases, there are many different strategies to involve a degradable linkage into a polymer backbone. The degradable linkage can be located (i) in the center of a homopolymer chain, (ii) as a junction in a block copolymer chain (iii), as multi-cleavable bonds along the polymer backbone (iv) in every repeat unit of the polymer chain, or (v) in the case of a block copolymer as cleavable bonds in every repeat unit of the one block. In the case of polymers with side chains the degradable linkage can be located either (vi) in the middle of the side chain or (vii) as a junction between the main-chain and the side chain.

The nature of the environmental stimulus can be classified into three categories: physical, chemical, and biomedical (**Table 1.2**) Polymer systems which respond to one or more stimuli, have been extensively used for the development of novel “smart” drug delivery systems. These systems are characterized as “smart” because they can release their cargo upon the remote and spatiotemporal control of their response to the applied stimulus. Another important fact is that the nanocarriers which can be degraded into small and non-toxic molecules in the presence of an applied stimulus are even more attractive for biological use [47], [48].

Table 1.2. Different types of stimuli.

Physical	Chemical	Biological
Temperature	pH	Enzyme substrate
Electromagnetic radiation	Specific ions	Other biochemical agents
Light	Chemical agents	
Electric fields		
Mechanical strength		
Sonic radiation		
Magnetic fields		

1.6 Polyhydrazones – Polyacylhydrazones as pH- and photo-degradable polymers

1.6.1 pH-degradable polymers

Acid-degradable polymers have been widely investigated and exploited in drug delivery applications among the various stimuli-degradable polymers that are accessible. The growing interest on pH-responsive systems can be traced back to the period when specific characteristics of the tumor microenvironment were discovered. It is widely known that in different tissues and cellular compartments the pH ranges. Due to the enhanced glycolysis in cancer cells, the microenvironment in cancer tissues is mildly acidic, 0.5-1.0 pH values lower compared to the normal tissues. Moreover, a larger decrease in the pH is observed in the intracellular organelles ranging from pH 6.3 in the early endosome to pH 4.7 in the lysosome [49]. This characteristic can be ideally exploited by acid-degradable carriers to trigger the selective release of anticancer drugs in tumor tissues or within the tumor cells [50], [51].

Acid-degradable polymers are those that contain in their polymer chain at least one acid-labile linkage. There is a wide range of chemical bonds that are known to be unstable under acidic conditions. However, only a few of them exhibit an enhanced degradation or hydrolysis rate in the presence of slightly acidic conditions, while being stable at neutral pH. This unique feature is determined by the chemical structure of the bond. Esters and orthoesters [52] , acetals or ketals [53], hydrazones [54] and imines [55] are the most commonly used acid-labile linkers.

Among them, hydrazones and acylhydrazones are acid-sensitive bonds, typically formed by the reaction of a carbonyl moiety (aldehyde or ketone) with a hydrazine or hydrazide group,

respectively, under mild conditions. The synthesis of hydrazones can be also accomplished by two more synthetic pathways: (a) the Japp–Klingemann reaction in which aryl diazonium salts and beta-keto esters or acids are coupled to form the hydrazones, and (b) the reaction between aryl halides and non-substituted hydrazones. The hydrazones synthesized using all three methods are generally crystalline and precipitate from the reaction mixture, which makes their purification process easy [50]. Synthesis of almost all the hydrazone linkages in the reported pH-responsive conjugates has been carried out by the condensation between the hydrazide groups of various copolymers with the ketone or aldehyde groups of the drugs.

The structure of a hydrazone (**Figure 1.6**) reveals that it has (i) an imine carbon that has both electrophilic and nucleophilic character, (ii) configurational isomerism stemming from the intrinsic nature of the C=N double bond, (iii) nucleophilic imine and amino-type (more reactive) nitrogen atoms, and (iv) in most cases an acidic N – H proton [56].

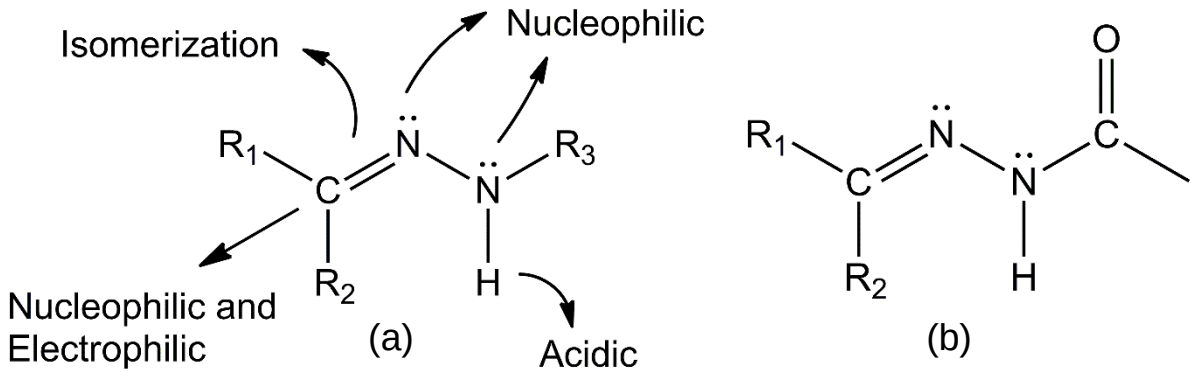

Figure 1.6 The structural composition of the hydrazone (a) and acyl-hydrazone (b), functional groups.

The hydrazone linkages, being pH-sensitive, find applications in drug delivery due to their faster hydrolysis rate at acidic pH relative to neutral physiological pH. The plausible mechanism involved in the hydrolytic breakdown of a hydrazone linkage at acidic pH is shown in **Figure 1.6** [57]. Various hydrazone linkages formed by the conjugation of the ketone group of doxorubicin (DOX), an anticancer drug, with hydrazides have been investigated by Greenfield and co-worker [58]. Another impressive feature of the (acyl)hydrazone bonds is their dynamic character. The (acyl)hydrazone bond is characterized as a dynamic covalent bond because of its ability to

reversibly form and break under mild conditions. Cleavage of the (acyl)hydrazone bond produces the initial molecules without the generation of any toxic by-products. Due to this unique property, several research groups have used these covalent bonds in the development of dynamic materials including self-healing polymers, adaptable polymer networks, shape-memory materials and others [51–54].

Figure 1.6. Acid-catalyzed hydrolysis of the hydrazone bond.

Despite all these interesting and promising characteristics of the (acyl)hydrazone bond, linear, main-chain polyhydrazones and polyacylhydrazones belong to a polymer family that has been barely studied in the literature. The major difficulty results from their insolubility in commonly used organic solvents polar and non – polar, an indication of extensive hydrogen bonding between the chains. The low solubility of the starting dihydrazide molecules also poses a problem in conventional solvents [55, 56].

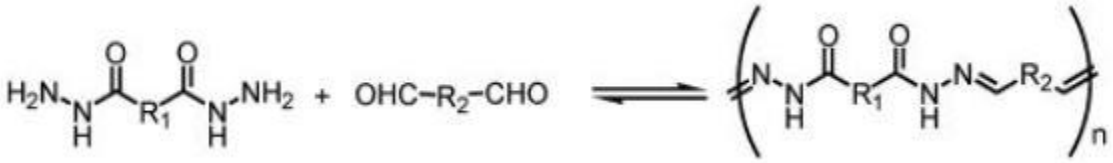

Figure 1.7. Polyacylhydrazone formation by condensation of a dihydrazide with a dicarbonyl compound; here, a dialdehyde.

1.6.2 Photo-degradable polymers

Among the various chemical and physical stimuli (e.g., pH, temperature, enzymes, ultrasound) employed to trigger the degradation of the polymer chains, light-degradable polymers have attracted considerable interest. Light, as an external stimulus, offers unique advantages like spatiotemporal control, as well as tunability of the irradiation wavelength and intensity [65]. So far, the great majority of photodegradable polymers rely on the light-induced cleavage of specific

chemical bonds, such as ester, triazine, ketal/acetal and urethane, which are accompanied by certain photo-absorbing moieties, namely, o-nitro benzyl (ONB) groups, coumarin derivatives or other aromatic units. The photolabile bonds are usually located either within the pendant groups of the polymer chain or as one single photocleavable bond at a junction point of two long polymer chains. However, the degradation of such materials results in the production of high molecular weight photo-products, which hinder their use in biomedical applications in which the removal of the by-products from the living organisms is crucial. On the other hand, photodegradable polymers bearing multiple photo-cleavable groups along their main-chain, to produce small molecule photo-products upon irradiation, are limited [66], [67]. In 2011, our group introduced for the first time a new class of photodegradable polymers, based on poly(ketals/acetals), exhibiting main-chain scission at incredibly low irradiation doses (10 mJ cm^{-2}) compared to other polymeric materials [68], [69] . More recently, Kowollik and co-workers reported the synthesis of main-chain photodegradable polyurethanes by introducing ONB moieties along the backbone of a polyurethane chain, and studied the degradation profiles of these materials both in solution and in thin films using a nanosecond pulsed laser at 340 nm [70].

1.7 Current Study

In this study, we designed a linear, main-chain, light-cleavable polyacylhydrazone which was used in the development of photo-degradable polymer-drug conjugates and prodrug nanoparticles. The polymer was synthesized via the step-growth copolymerization of adipic acid dihydrazide with dibenzaldehyde terminated poly(ethylene glycol) (PEG_{ald}), under mild acidic conditions, to afford a hydrophilic PEG-*alt*-adipic acid (PEG-*alt*-AA) alternating copolymer (Scheme 1b). The PEG_{ald} macromonomer was prepared by the esterification of HO-PEG-OH with 4-carboxybenzaldehyde (Scheme 1a).

The main-chain photo-degradation of the resulting copolymer, upon irradiation at $\lambda = 254$ nm with a very low power density, 0.1mW cm^{-2}, in dimethylsulfoxide (DMSO) and water, was investigated. Copolymers with a hydrazide end-group were prepared using an excess of the adipic acid dihydrazide comonomer during the polymerization. Next, the hydrophobic model anticancer drug, doxorubicin (DOX), was linked to the hydrazide end-groups of the polymer via acylhydrazone linkages, to produce amphiphilic PEG-*alt*-adipic acid-DOX (PEG-*alt*-AA-DOX) drug conjugates (Scheme 1c). Doxorubicin has been used as a model drug being a potent antineoplastic agent able to intercalate DNA and to induce apoptosis. Doxorubicin is the first chemotherapeutic agent

used for the treatment of breast cancer, sarcomas, leukemia, Hodgkin's disease and many other tumors. Moreover, it is characterized by a red auto-fluorescence which facilitates its localization.

The conjugates were afterwards self-assembled in water to form spherical, micellar structures evidenced by scanning and transmission electron microscopies. Following irradiation of the micellar structures with UV light, the assemblies were disrupted, due to the photolysis of the acylhydrazone bonds along the polymer backbone, and the drug molecules were released. The synergistic action of the two stimuli, pH and light irradiation, augmented the disruption of the self-assembled prodrug nanostructures and the drug release.

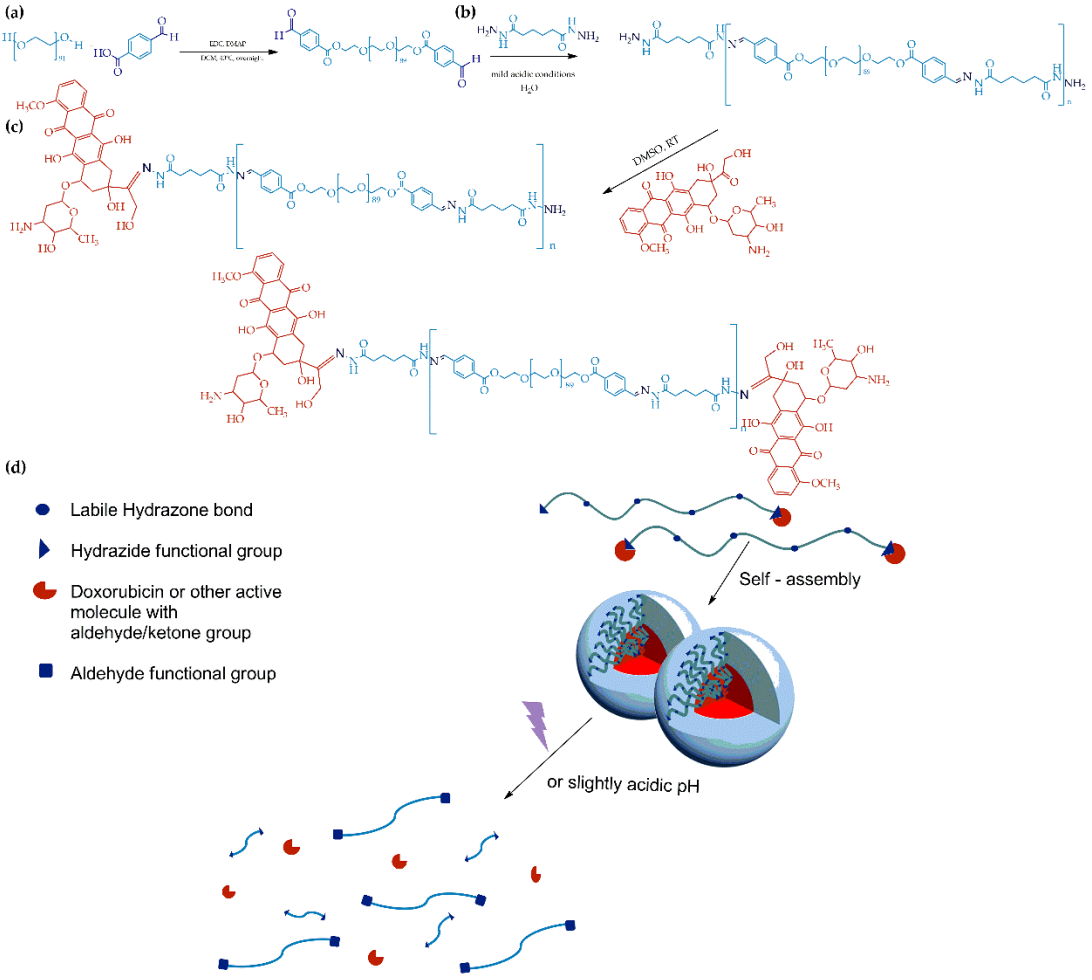

Scheme 1. Synthetic routes for the preparation of the (a) PEG_{ald} macromonomer, (b) PEG-*alt*-AA alternating copolymer, (c) PEG-*alt*-AA-DOX drug conjugate; (d) schematic representation of the self-assembly process of the PEG-*alt*-AA-DOX conjugates and the pH- and/or light-induced disruption of the assemblies.[71]

Chapter 2

Experimental

2.1 Materials

Diethyl ether, petroleum ether, n- hexane (96%) and dichloromethane (DCM) were obtained from Scharlau. 4-carboxybenzaldehyde (98%) and triethylamine (TEA, 99+%) was purchased from Alfa Aesar. Benzoic acid was obtained from AppliChem. 1-ethyl-3-(3-dimethylaminopropyl) carbodiimide (EDC, ≥ 97%), 4-(dimethylamino)pyridine (DMAP, 99%), adipic acid dihydrazide (≥ 98%) and poly(ethylene glycol) (Mn = 4000 gr mol^{-1}) were obtained from Sigma Aldrich and doxorubicin hydrochloride salt (DOX·HCl, > 99%) was purchased from LC Laboratories. DCM was dried over calcium hydride. DMSO (99.9%) was obtained from Fisher Chemical and ethanol (≥ 98%) from Honeywell. For the preparation of all samples was used Milli-Q water, with a resistivity of 18.2 MΩ·cm at 298 K, obtained from a Millipore apparatus.

2.2 Characterization methods

2.2.1 Size Exclusion Chromatography

A Waters size exclusion chromatography (SEC) instrument comprising a Waters 515 isocratic HPLC pump, two Mixed-D and Mixed-E (Polymer labs) columns, a Waters 2745 Dual absorbance detector and a Waters 410 refractive index (RI) detector was used for the determination of the molecular weights (M_n) and the molecular weight distributions (M_w/M_n) of the polymers. THF (containing 2 v/v% triethylamine) was used as the eluent at a flow rate of 1 mL min^{-1}. The calibration curve was based on six narrow poly(methyl methacrylate) (PMMA) standards with molecular weights ranging from 625 to 138,000 g mol^{-1}. To prepare the samples for SEC, the polymers were dissolved in THF at a concentration of 15 mg mL^{-1}, the polymer solutions were filtered through 0.45 μm pore size PTFE syringe filters and were injected into the system.

2.2.2 ^{1}H NMR spectroscopy

^{1}H Nuclear Magnetic Resonance (^{1}H NMR) spectra were recorded on two Brucker 300 MHz and 500 MHz spectrometers using $CDCl_3$ or DMSO-d_6 as the solvents.

2.2.3 ATR-FTIR spectroscopy

Nicolet 6700 spectrometer (Thermo Fisher Scientific, Waltham, MA, USA) was utilized to record attenuated total reflection-Fourier transform infrared (ATR-FTIR) spectra. For each spectrum, 64 scans were collected in the 500–4000 cm^{-1} range.

2.2.4 Ultraviolet/Visible spectroscopy

Ultraviolet-visible (UV-vis) absorption spectra were recorded on a Shimadzu UV-2600 spectrophotometer in the wavelength range of 200-600 nm. The samples were prepared by the dissolution of the polymers or polymer-DOX conjugates in DMSO or H_2O (pH 7.4) at a concentration of 10^{-3} mg mL^{-1}.

2.2.5 Dynamic Light Scattering (DLS)

A Malvern Zetasizer Nano ZS instrument equipped with a He-Ne laser (λ = 633nm) at a 90° scattering angle, was used for the dynamic light scattering (DLS) measurements. Before each measurement, the sample was filtered through a 0.45 μm pore size hydrophilic, cellulose acetate syringe filter. The measurements were conducted at 25 °C. The reported data are average values of three runs. The size of the micelles was measured.

2.2.6 Field emission scanning electron microscopy (FE-SEM) and Transmission electron microscopy (TEM)

The size and the morphology of the self-assembled structures were characterized by field emission-scanning electron microscopy (FE-SEM), using a JEOL JSM-7000F microscope and by transmission electron microscopy (TEM), using a JEOL JEM-2100 microscope. Samples were prepared by the deposition of a drop of a dilute polymer solution on a glass substrate for SEM or a carbon coated copper grid for TEM, and were dried overnight at 25 °C.

2.2.7 Fluorescence Spectroscopy

The fluorescence measurements were recorded on a Lumina Fluorescence Spectrometer (Thermo Scientific) equipped with a 150 W CW Xenon-arc lamp. The excitation and emission slits were maintained at 10 nm. The fluorescence spectra of DOX and the PEG-*alt*-AA-DOX conjugate were recorded from 370 nm to 600 nm upon excitation at 367 nm, whereas, the respective spectrum of the copolymer was recorded upon excitation at 302 nm. All samples were measured at room temperature.

2.3 Synthesis of the dibenzaldehyde terminated poly(ethylene glycol) (Mn = 4000 gr/mol) macromonomer

4-carboxybenzaldehyde (0.3 gr, 2 mmol) and EDC (0.23 gr, 1.5 mmol) were dissolved in 20 mL anhydrous DCM and were stirred at 40 °C for 30 min, followed by the addition of DMAP (0.36 gr, 3 mmol) and HO-PEG-OH (2 gr, 0.5 mmol). The reaction was stirred at 40 °C for 24 h. Next, the product was precipitated in diethyl ether, washed 10 times with petroleum ether and dried overnight under vacuum at room temperature (RT). The dried product was dissolved in chloroform and filtered through a 0.45 μm PTFE filter to remove the unreacted 4-carboxybenzaldehyde. Finally, it was precipitated again in diethyl ether and dried overnight under vacuum to obtain PEG_{ald} at 82.5% yield.

2.4 Synthesis of the PEG-*alt*-AA alternating copolymer

Adipic acid dihydrazide (25 mg, 0.14 mmol) was dissolved in 2 mL milli-Q water. The monomer solution was placed in a sonication bath until complete dissolution. Next, PEG_{ald} (0.5 gr, 0.12 mmol) was added to the solution, followed by the addition of 2-3 drops of 0.1 N HCl. The reaction was left under stirring for 24 h at 25 °C. The next day, the solvent was evaporated using a rotary evaporator and the reaction was dried under vacuum at RT. The white solid was dissolved in chloroform and was purified by fractional precipitation in hexane. The final copolymer was stored under a N_2 atmosphere at 4 °C until use.

2.5 Acidic hydrolysis of the PEG-*alt*-AA alternating copolymer

A 20 mg mL^{-1} PEG-*alt*-AA alternating copolymer solution in water was prepared, its pH was adjusted at 5.2, using 0.1 N HCl solution, and it was kept under stirring at 37 ^{o}C. The hydrolysis of the copolymer was monitored by SEC after 5 days under the effect of pH. Moreover, a 0.02 mg mL^{-1} of the above copolymer solution was prepared, and the acidolysis was monitored by measuring the absorption of the polymer solution at predesigned time intervals by UV-vis spectroscopy.

2.6 Synthesis of a small molecule acylhydrazone analogue

Adipic acid dihydrazide (0.1 gr, 0.57 mmol) was dissolved in 4 mL ethanol. The solution was first sonicated for 10 min and then stirred for 10 min in a water bath at 40 °C until complete dissolution. Next, a solution of 4-carboxybenzaldehyde (0.17 gr, 1.14 mmol) in 2 mL ethanol was prepared. The two solutions were mixed and a white solid precipitated instantly. The reaction was stirred for another 3 h before filtering off the white solid product and washing it with a large amount of ethanol and water. The final product was dried overnight under reduced pressure at RT.

2.7 Synthesis of the PEG-*alt*-AA-DOX drug conjugate

First, DOX·HCl (2 mg, 0.003445 mmol) was dissolved in DMSO (2.5 ml) and TEA (3 µL) was added to neutralize the HCl. After 20 h stirring at RT, the hydrophobic DOX was obtained. Next, the PEG-*alt*-AA copolymer (0.05 g, 0.00179 mmol) was added to the DOX solution and the reaction mixture was stirred for 20 h, before being transferred to a dialysis membrane with a molecular weight cut-off of 3500 Daltons. The mixture was dialyzed against DMSO to remove the unreacted DOX molecules. The conjugated DOX molecules were quantified by fluorescence spectroscopy using a standard calibration curve of DOX in DMSO and the drug loading was calculated using equation 1 below:

$$\% \text{ Drug loading} = \frac{\boldsymbol{conjugated\ CPT\ (gr)}}{\boldsymbol{weight\ of\ polymer\ (gr)}} \times \mathbf{100} \qquad (1)$$

2.8 Self-assembly of the amphiphilic PEG-*alt*-AA-DOX drug conjugates in water

A solution of the PEG-*alt*-AA-DOX conjugate (5 mg mL^{-1}) in 5 ml DMSO was prepared. Next, 15 ml water (pH 7.4) were added in the solution under vigorous stirring at a rate of 0.1 ml min^{-1} using a syringe pump. Afterwards, the solution was dialyzed against water using a dialysis membrane with a molecular weight cut-off of 3500 Daltons to remove the organic solvent. The final solution was filtered through a 0.45 μm pore size cellulose acetate syringe filter and was kept at 4 °C until use.

2.9 Photoirradiation experiments

All photoirradiation experiments were performed using a UV lamb at 254 nm and a power density of 0.1 mW cm^{-2}. The samples were transferred to a quartz cuvette and were placed at a distance of 1 cm from the lamp. The % photodegradation of the small molecule acylhydrazone, the PEG-*alt*-AA alternating copolymer and the self-assembled PEG-*alt*-AA-DOX drug conjugate was calculated from the recorded UV-visible spectra by monitoring the decay of the maximum absorption band. For the calculations the following equation was used:

$$\% \text{ Photodegradation} = \frac{A_0 - A_t}{A_0} \times 100 \qquad (2)$$

Where, A_0 and A_t is the maximum absorbance of the acylhydrazone (λ = 302 nm), the PEG-*alt*-AA alternating copolymer (λ = 302 nm) or the PEG-*alt*-AA-DOX conjugate (λ = 297 nm), before and after irradiation for different time intervals (t), respectively.

2.10 In vitro acid- and photo-triggered drug release

An aqueous solution of the self-assembled PEG-*alt*-AA-DOX conjugate (2.5 mg ml^{-1}, 3 ml) was transferred into a dialysis bag with molecular weight cut-off of 3500 Daltons and was immersed in 10 ml H2O at pH 5.2 under gentle stirring (100 rpm) at 37 °C. Next, the sample was irradiated at 254 nm for 5 min at predesigned time intervals. After each irradiation cycle, the solution was stirred for 15 min and then the aqueous medium was collected and replaced with fresh water (10 ml). The collected samples were dried, first using the rotary evaporator and then under vacuum for 20 h. The dry samples were dissolved in DMSO (2.5 ml) and their fluorescence spectra were recorded. The concentration of DOX in each sample was determined using a standard calibration curve of DOX in DMSO. The % DOX released was calculated using the following equation:

$$\%\ \boldsymbol{DOX\ release} = \frac{C_t + C_{t-1}}{C_{total}} \times 100 \qquad (3)$$

Where, C_t and C_t-1 are the concentrations of DOX at two successive irradiation time intervals and C_{total} is the initial concentration of DOX in the self-assembled conjugate.

Chapter 3

Results and Discussion

The main-chain polyacylhydrazones were synthesized via a typical step-growth copolymerization of a dihydrazide and a dialdehyde. Adipic acid dihydrazide was chosen because it is a small, hydrophilic molecule that has been previously used in the biomedical field [32,33]. The second comonomer, is a macromonomer, poly(ethylene glycol) (PEG) (Mn = 4000 gr/mol), which is hydrophilic, non-toxic and FDA approved. Moreover, it is well known for its stealth properties and has been extensively used in drug delivery [34,35]. To introduce the photosensitive moieties and the aldehyde end-groups required to react with the hydrazide functionalities of adipic acid, dihydroxy-functional PEG (HO-PEG-OH) was esterified with 4-carboxybenzaldehyde.

3.1 Synthesis and Characterization of the dibenzaldehyde terminated poly(ethylene glycol) (Mn = 4000 gr/mol) macromonomer PEG_{ald}.

Synthesis of PEG_{ald} was achieved by a simple Steglich esterification reaction between the hydroxyl groups of dihydroxy – functional PEG (HO-PEG-OH) and the carboxylic acid groups of 4-carboxybenzaldehyde as discussed above in Chapter 2. To initiate the reaction, EDC was used to activate the carboxylic acid group and form the O-acylisouria intermediate followed by the addition of DMAP in catalytic amounts which rapidly reacted with O-acylisourea to form an acyl pyridinium species incapable of intramolecular by-product formation, and which can react with the alcohol to form the desired ester. This chemical reaction is shown below in **Scheme 3.1**.

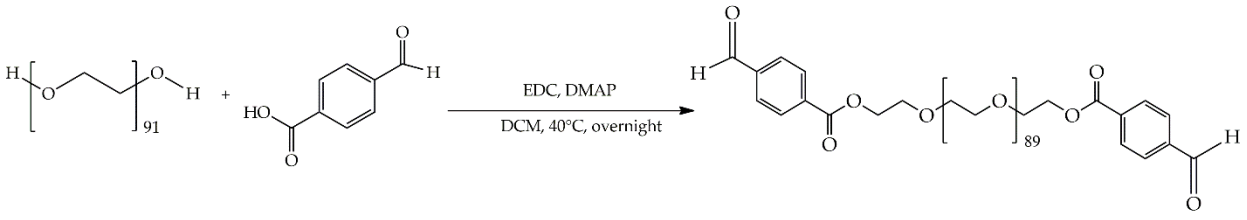

Scheme 3.1. Synthetic route for the preparation of the macromonomer PEG_{ald}.

The synthesized PEG_{ald} was characterized by ^1H NMR and ATR-FTIR spectroscopies and SEC. The ^1H NMR spectrum of PEG_{ald} (**Figure 3.1**) shows an intense peak at δ 3.67 ppm (H1) assigned

to the methylene protons of the monomer repeat units of PEG and two peaks at δ 3.87 ppm and δ 4.53 ppm (H2 and H3) assigned to the methylene protons next to the newly formed ester bonds, verifying the successful derivatization of the polymer end-groups. In addition, the presence of a peak at *δ* 10.13 ppm which corresponds to the aldehyde protons (Ha) and the peaks at *δ* 8.0 and 8.24 ppm attributed to the aromatic protons (Hb and Hc) of the benzaldehyde group, confirm the presence of the aromatic aldehyde functionalities at the two polymer chain ends [72].

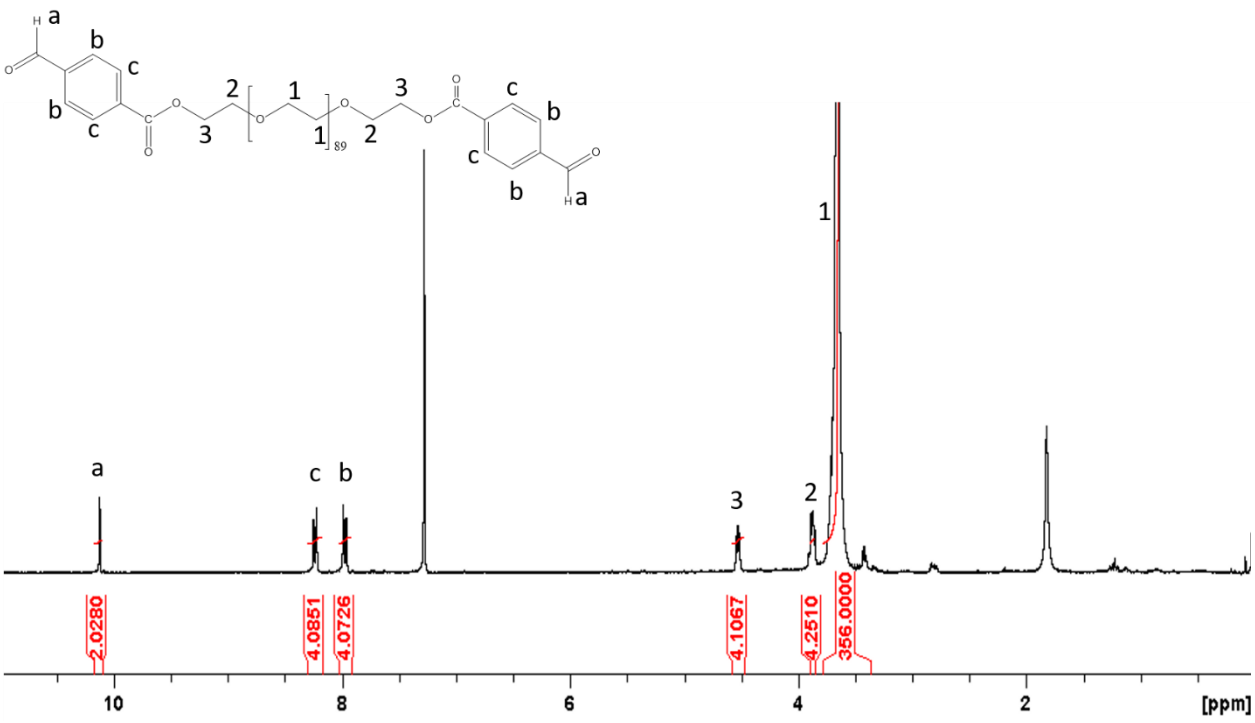

Figure 3.1. ^{1}H NMR spectrum of PEG_{ald} in $CDCl_3$.

Furthermore, the PEG_{ald} was characterized with ATR-FTIR spectroscopy [72], [73]. As shown in **Figure 3.2** the ATR-FTIR spectrum of PEG before esterification and the spectrum of the final product are pretty similar as expected. The broad band at 2900-2800 cm^{-1} represent the C-H stretching vibrations and is attributed to the alkyl chain of the polymer. Also, the peaks at 1460 cm^{-1} and 1100 cm^{-1} represent the C-H bending vibration, and at 1242 cm^{-1} the twisting bending vibration of C-H can be observed. The peak at 1100 cm^{-1} represents the C-O stretching vibrations.

As it can be seen, the spectrum of PEG_{ald} shows a new band at 1711 cm^{-1}, characteristic of the carbonyl bonds representing the C=O stretching, which is attributed to the aldehyde and ester groups introduced at the polymer chain ends and support the NMR results.

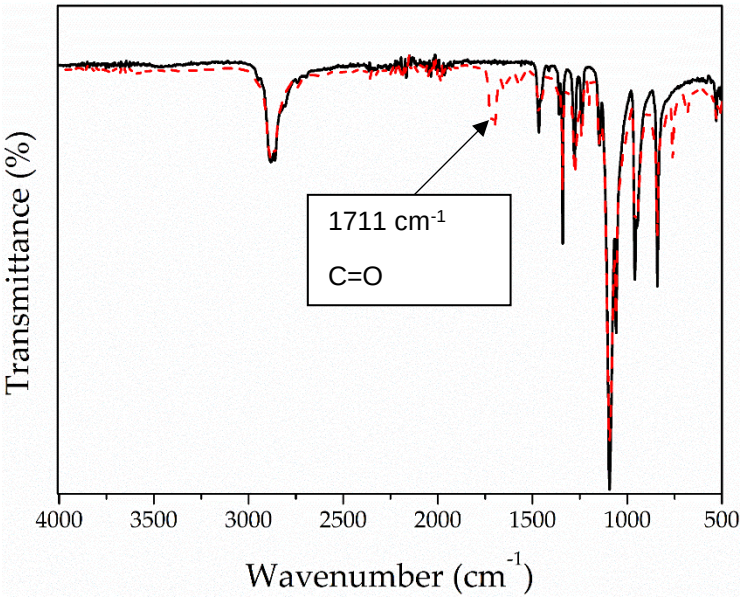

Figure 3.2. ATR-FTIR spectra of PEG before (black solid line) and after (red dashed line) esterification with 4-carboxybenzaldehyde.

Finally, the SEC traces of the PEG macromonomer (**Figure 3.3**), before and after esterification with 4-carboxybenzaldehyde were obtained. As shown below, the elution time of the polymer did not change significantly, after esterification as expected, because the MW difference between PEG and PEG_{ald} is only 600. Also the chromatogram obtained, demonstrated the absence of chain degradation during the end-group esterification reaction.

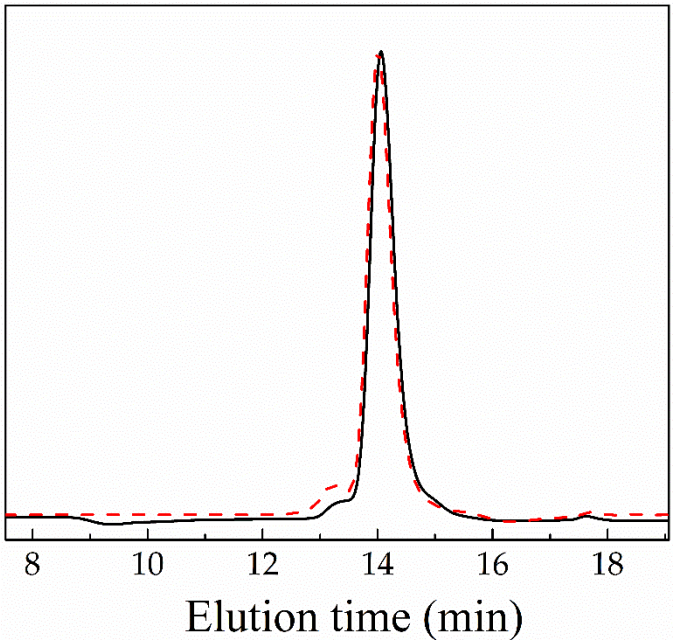

Figure 3.3. SEC traces of PEG before (black solid line) and after (red dashed line) esterification with 4-carboxybenzaldehyde.

3.2 Synthesis and characterization of the PEG-*alt*-AA alternating copolymers

For the synthesis of the alternating polyacylhydrazone copolymer (PEG-*alt*-AA), the two comonomers, PEG_{ald} and adipic acid dihydrazide, were reacted at 1:1.2 molar ratio in order to ensure the presence of the hydrazide groups at the end groups of the copolymer. The polycondensation reaction takes place between the hydrazide groups of adipic acid dihydrazide and the aldehyde groups of the PEG_{ald} macromonomer.

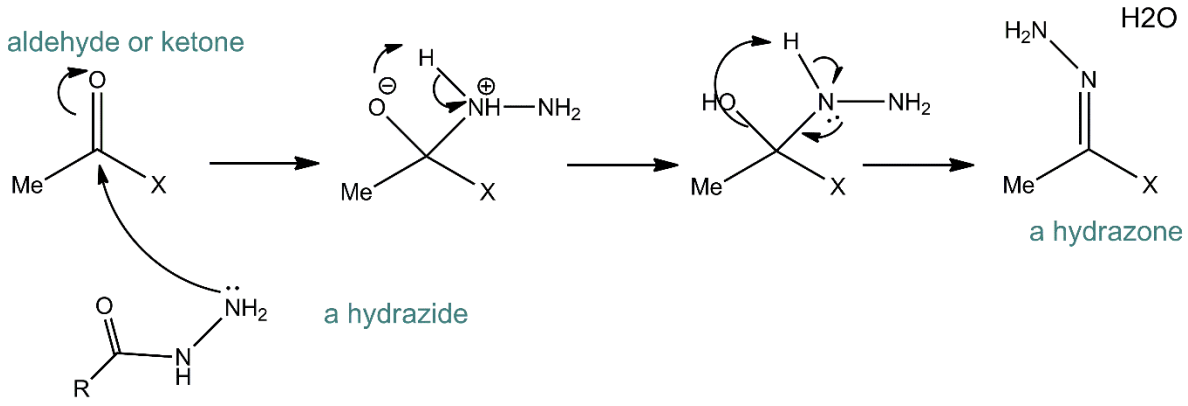

Scheme 3.2. Reaction mechanism of hydrazone formation.

3.2.1 SEC characterization of the PEG-*alt*-AA alternating copolymer

SEC analysis of the polyacylhydrazone polymer prepared (**Figure 3.4**) showed a peak which was shifted to lower elution times, compared to the PEG macromonomer, verifying the synthesis of the alternating copolymer.

As it can be observed from the SEC traces above, after the polymerization unreacted monomers remain in the reaction mixture. In order to purify the resulting polymer two fractional precipitations were carried out. The final purified polymer had a M_n = 28,000 gr mol^{-1} and M_w/M_n = 1.21. The molar mass of the copolymer is quite high and its molecular weight distribution is relatively narrow, given the nature of the condensation polymerization. In a polycondensation reaction, the monomers react in a non-controlled manner to form oligomers and the oligomers react to form the polymer chains. Due to the non-controlled character of the polymerization and the stoichiometric imbalance of the comonomers, mentioned above, the final polymers had high polydispersity indexes (M_w/M_n > 1).

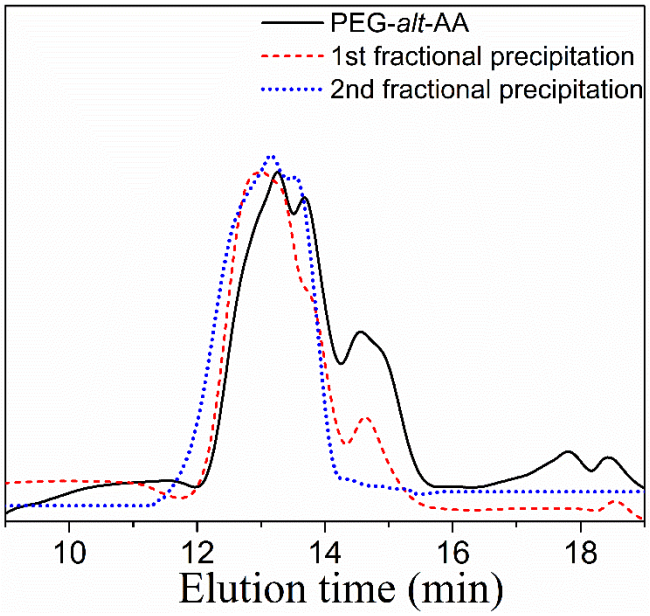

Figure 3.4. SEC traces of the PEG-*alt*-AA polymer before precipitation (black solid line), after onw fractional precipitation (red dashed line) and after two fractional precipitations (blue dotted line).

The progress of the polycondensation reaction was monitored by recording the SEC chromatograms at different polymerization times. **Figure 3.5** shows the kinetics of the polymerization at 0 min, 2 h and 24 h. As shown below, the polymerization occurs rapidly within a few seconds and it does not proceed further (the SEC traces at 0 min and 24 h do not differ significantly in their elution times).

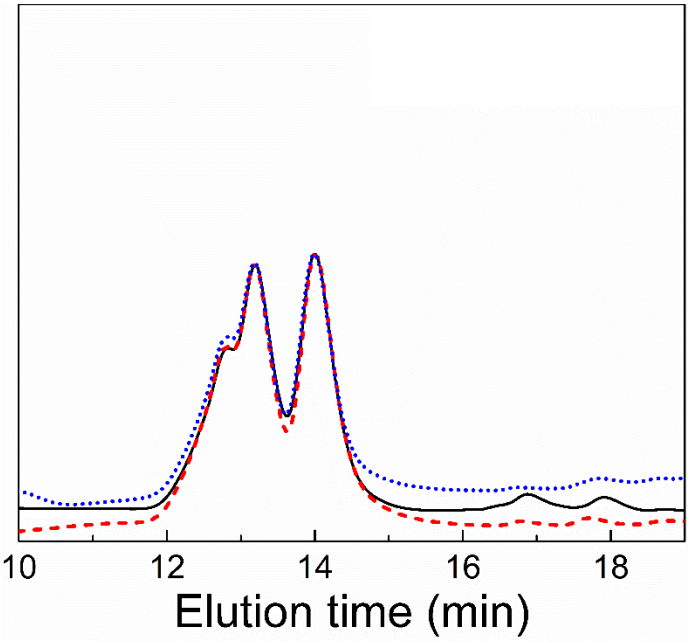

Figure 3.5. SEC traces of the PEG-*alt*-AA polymer at 0 min reaction time (black solid line), 2 h reaction time (red dashed line) and 24 h reaction time (blue dotted line).

This can be explained by the aromatic groups of the PEG_{ald} macromonomer and the electron withdrawing groups (-C=O) of the adipic acid dihydrazide monomer, that make the constant of hydrazone formation several times higher [74].

It has been already reported in the literature that the reaction rate for the formation of a hydrazone bond, is affected by the presence of an acid catalyst [63]. Herein, we observed that the polymerization occurs within seconds at natural pH 7.2. However, in order to investigate the effect of acid, the polymerization kinetics as a function of the solution pH were monitored by SEC (**Figure 3.6**). All polymerization reactions were terminated after 2 h. As observed, between pH 4.5 and 5.2, the average M_w of the resulting polymers increases as the pH decreases. These observations are in good agreement with the reaction mechanism itself, as the acid-catalyzed dehydration of the tetrahedral intermediate is typically the rate-determining step. Although the

reaction rate for hydrazone formation can be greatly accelerated under acidic conditions, the reaction slows down again if the pH of the reaction medium is too low. This is due to the fact that the nucleophile is in equilibrium with two different protonation states (**Scheme 3.3**). Hydrazines can become protonated at both their nitrogen atoms, forming hydrazinium ion a and b, respectively. These protonated species do not lead to product formation, due to their low nucleophilicity and thus, the reaction slows down at more acidic pH (typically under pH 3) [75].

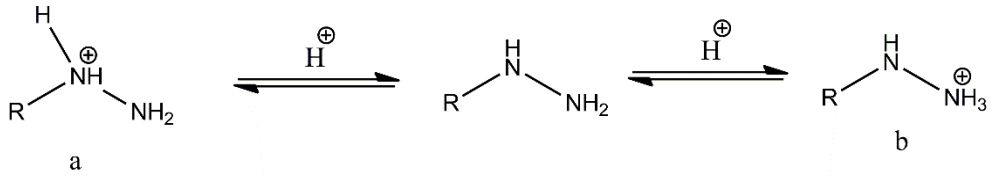

Scheme 3.3. Equilibrium between the nucleophiles and the respective protonated species.

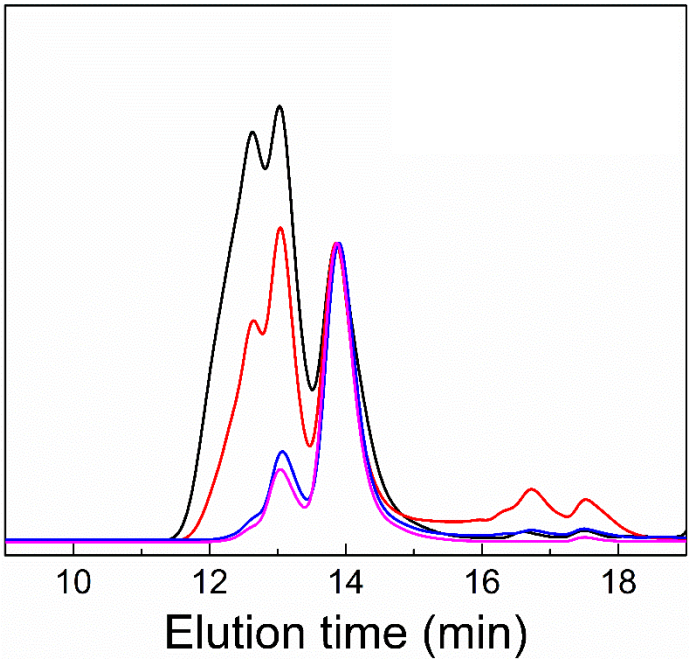

Figure 3.6. SEC traces of the PEG-*alt*-AA polymer formed at different pH values, pH 4.5 (black line), pH 5.2 (red line), pH 3.1 (blue line) and pH 2 (magenta line).

3.2.2 ^{1}H NMR characterization of the PEG-*alt*-AA alternating copolymer

Moreover, the ^{1}H NMR spectrum of the product (**Figure 3.7**) was recorded. The peaks attributed to the protons of both the PEG and the adipic acid dihydrazide comonomer repeat units can be

clearly seen at δ 3.67 ppm (Hg), 3.87 ppm (Hf), 4.53 ppm (He), 7.8 ppm (Hd), 8.0-8.21 ppm (Hc) and at δ 2.02 ppm (Hi), 2.26 ppm, 2.68 ppm (Hh), respectively. Also, the characteristic peak at δ 11.42-11.52 ppm (Ha), which is attributed to the hydrazone protons, confirm the SEC results discussed above. It should be noted that the absence of the peak of the aldehyde proton of PEG_{ald} at δ 10.13 ppm, suggests the quantitative reaction of PEG_{ald} with the dihydrazide comonomer which is in excess in the reaction.

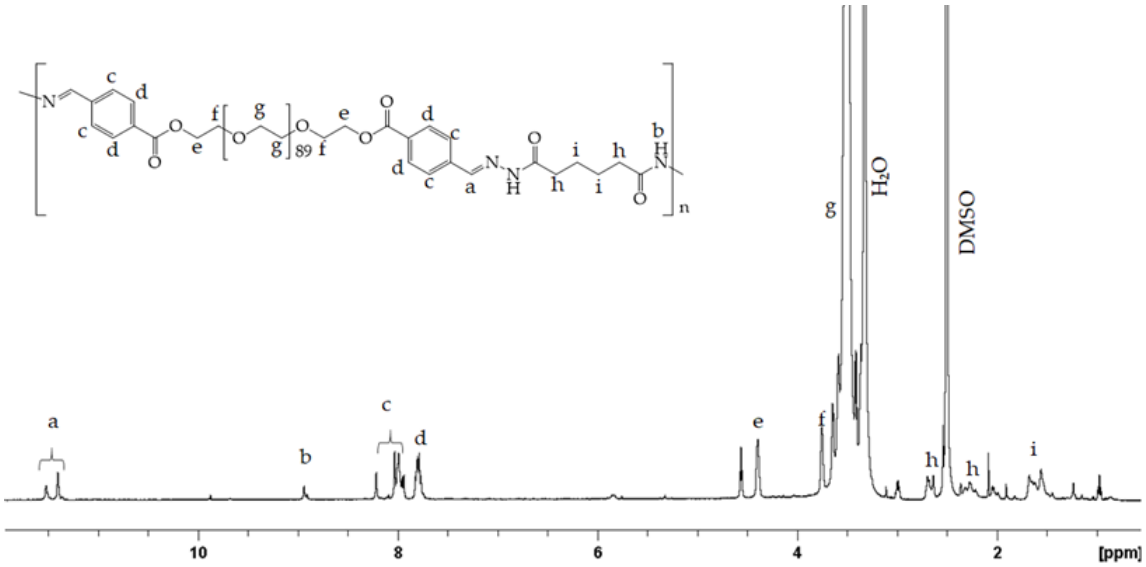

Figure 3.7. ^{1}H NMR spectrum of the PEG-*alt*-AA alternating copolymer in DMSO-d^{6}.

3.2.3 ATR-FTIR analysis of the PEG-*alt*-AA alternating copolymers

The PEG-*alt*-AA alternating copolymer was characterized by ATR-FTIR spectroscopy. **Figure 3.8**, shows the ATR-FTIR spectra of adipic acid dihydrazide, the PEG_{ald} macromonomer and the PEG-*alt*-AA alternating copolymer. The characteristic vibration bands at 2869 cm^{-1}, 1694 cm^{-1} and 1095 cm^{-1}, assigned to the N-H, C=O and C-O stretching vibrations, respectively were observed in the spectrum of the alternating copolymer. More importantly though, the presence of the characteristic vibration band at 1600 cm^{-1}, which is attributed to the stretching vibration of the acylhydrazone bonds (C=N), in the spectrum of the copolymer and it's absence in the ATR-FTIR spectra of the two precursor comonomers, verified the successful synthesis of the polymeric product [76].

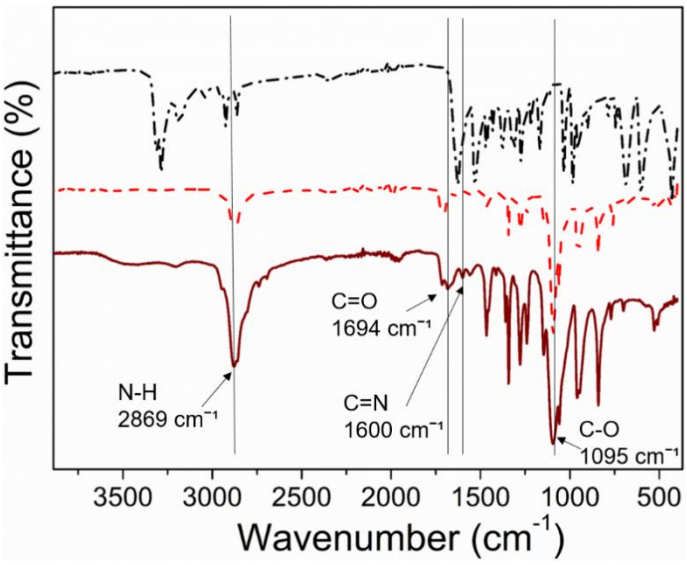

Figure 3.8. ATR-FTIR spectra of adipic acid dihydrazide (black dash dotted line), PEG_{ald} (red dashed line) and the PEG-*alt*-AA alternating copolymer (wine solid line).

3.3 pH-induced degradation of the PEG-*alt*-AA alternating copolymers

Acylhydrazone linkages have been proposed for several applications in the evaluation of drug delivery systems, due to their high cleavage rate at acidic pH compared to neutral physiological pH values, as discussed in Chapter 1.6.1. In order to investigate the pH degradation process of the PEG-*alt*-AA alternating copolymers, a solution of the copolymer in water at pH 5.2 was prepared, to simulate the pH environment in tumor tissues, and was left under stirring. Samples were removed from the solution at regular time intervals, and the degradation profile of the copolymer was monitored by SEC and UV/vis spectroscopy.

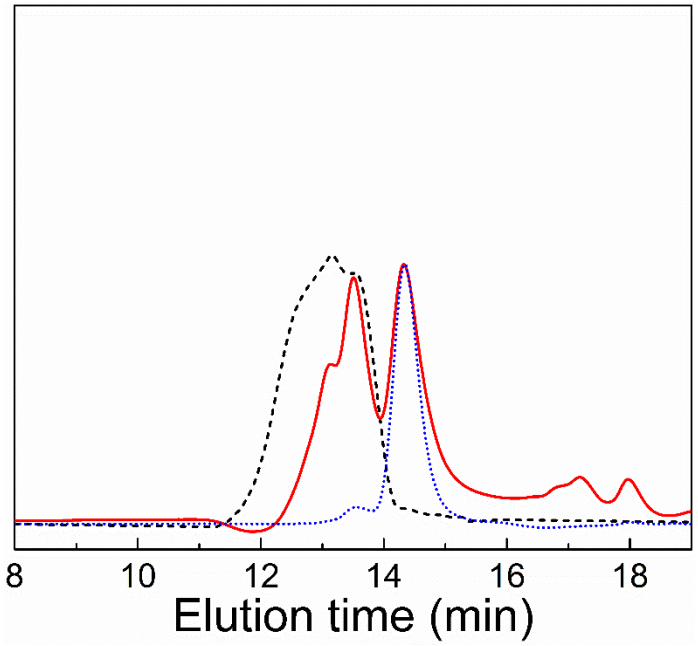

Figure 3.9. SEC traces of the PEG-*alt*-AA alternating copolymer as prepared (black dashed line), the PEG_{ald} macromonomer (blue dotted line) and the PEG-*alt*-AA after 5 days stirring at pH 5.2 (red solid line).

As shown in **Figure 3.9**, the copolymer peak decreased after 5 days stirring at pH 5.2, and a new peak appeared at higher elution times, which corresponds to the precursor PEG_{ald} macromonomer. Moreover, two new peaks appeared at much higher elution times (t = 16.5 to 18.5 min), indicating the formation of low molecular weight by-products. These peaks can be attributed to adipic acid dihydrazide and other low molecular weight products, however, their size were beyond the analytical range of SEC. The observed slow kinetics of the hydrolysis reaction of the copolymer is attributed to the resistance of the acylhydrazone bonds, derived from aromatic aldehydes and ketones, to the low solution pH due to the conjugation of the π electrons of the -C=N- bond of the hydrazone with the aromatic benzene ring [77].

The pH degradation of the copolymer was also investigated via UV-Vis spectroscopy. For this, a 0.02 mg ml^{-1} copolymer solution in H_2O at pH 5.2 was prepared and was left under stirring. The UV/vis absorption spectra of the sample were measured at different time intervals. **Figure 3.10** shows that at 0 min in pH 5.2 the absorption band of the copolymer was centered at ~302 nm and for the next 2 h no significant change was observed. After 23 h at pH 5.2, the absorbance of the peak decreased slightly, but no further indication of polymer degradation was observed. Finally, after 7 days under stirring at pH 5.2, a new peak at ~260 nm appeared which corresponds to the absorption band of the PEG_{ald} macromonomer, a result that strongly supports the pH-induce degradation process found by SEC as discussed above.

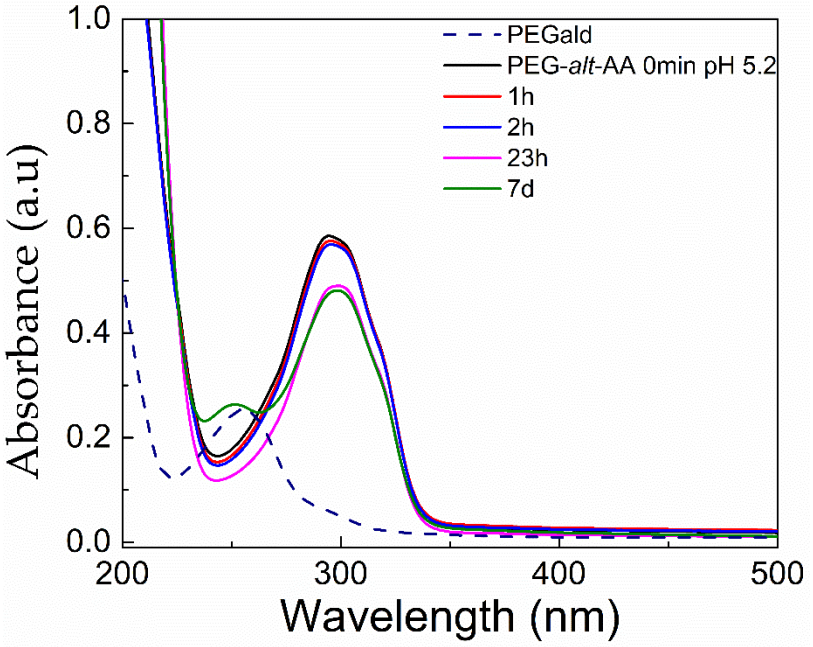

Figure 3.10. UV-vis absorption spectra of an aqueous PEG-*alt*-AA solution at pH 5.2 at different time intervals under stirring at 37°C.

3.4 Synthesis and photodegradation of a small acylhydrazone molecule

Before investigating the photodegradation behavior of the PEG-*alt*-AA copolymer, the photosensitivity of the aromatic acylhydrazone bonds was examined using a small diacylhydrazone molecule in a proof-of-concept study. For this, 4-carboxybenzaldehyde was reacted with adipic acid dihydrazide at a 2:1 molar ratio, to prepare a diacylhydrazone analogue (**Figure 3.11a**).

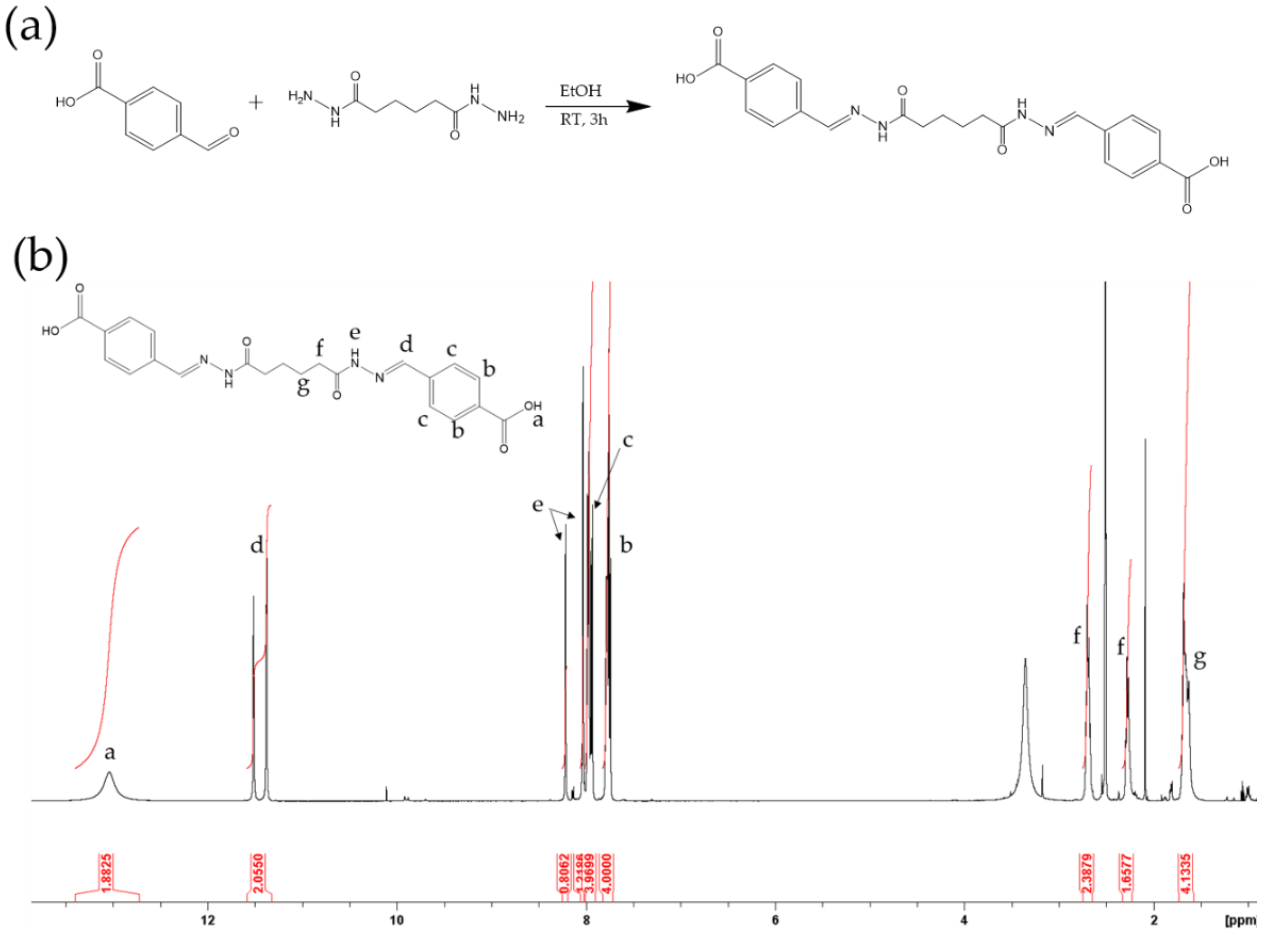

Figure 3.11. (a) Schematic representation of the synthetic procedure followed for the preparation of the small diacylhydrazone molecule and (b) ^{1}H NMR spectrum of the product in DMSO-d^{6}.

3.4.1 ^{1}H NMR characterization

In order to verify the successful synthesis of the diacylhydrazone molecule ^{1}H NMR spectroscopy was used (**Figure 3.11b**). The peaks at δ 1.67, 2.27 and 2.69 ppm and the peaks at δ 8.03-8.22 ppm can be attributed to the -CH_2- (Hg and Hf) and to the -NH- (He) protons of adipic acid

dihydrazide, respectively. In addition, the aromatic protons of 4-carboxybenzaldehyde are observed at δ 7.75-7.96 ppm (Hb and Hc) and the carboxylic acid proton (Ha) at δ 13.05 ppm. Furthermore, the ^{1}H NMR spectrum of the product showed the characteristic peaks at δ 11.37-11.51 ppm attributed to the acylhydrazone protons, verifying the successful synthesis of the diacylhydrazone derivative.

3.4.2 Photodegradation experiments of the small diacylhydrazone molecule

After its successful synthesis, a solution of the diacylhydrazone molecule in DMSO was subjected to light irradiation (254 nm, 0.1 mW cm^{-2}) and its degradation profile was monitored by UV-vis spectroscopy. Before irradiation the diacylhydrazone molecule exhibited a broad absorption band centered at ~302 nm (**Figure 3.12a**). After irradiation, the absorbance at 302 nm gradually decreased and a new peak at 254 nm eventually appeared, which coincided with the absorption band of 4-carboxybenzaldehyde, verifying the photo-induced cleavage of the acylhydrazone bonds. The kinetics of the photodegradation process were determined from the decrease in the absorption intensity at 302 nm as a function of irradiation time (**Figure 3.12b**), and showed that ~45% of the acylhydrazone bonds were cleaved after only 10 min irradiation, whereas the degradation of the bonds was slowed down for longer time intervals reaching ~65% cleavage after ~ 2 h irradiation.

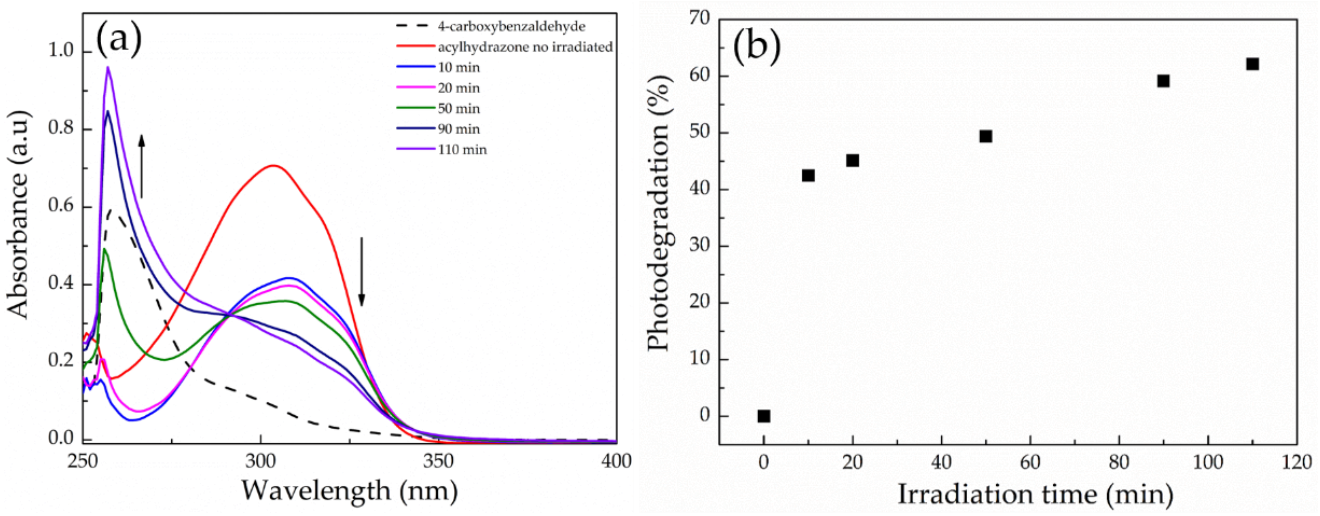

Figure 3.12. (a) UV-vis absorption spectra of a 0.02 mg ml^{-1} solution of the small diacylhydrazone molecule in DMSO upon irradiation at 254 nm and (b) % photodegradation of the diacylhydrazone as a function of irradiation time.

3.5. Photodegradation of the PEG-*alt*-AA alternating copolymers

Having determined the photosensitivity of the aromatic acylhydrazone linkages, the photo-induced breakdown of the PEG-alt-AA alternating copolymer was explored using SEC to detect the changes in polymer molar mass upon light irradiation, and was further analyzed using UV-Vis spectroscopy.

3.5.1 Photodegradation of the PEG-*alt*-AA alternating copolymers monitored by SEC

As observed in **Figure 3.13**, after 1 h irradiation at 254 nm, the copolymer peak decreased substantially, and a new peak, which coincides with that of the precursor PEG_{ald} macromonomer, emerged in the SEC trace of the polymer. Furthermore, at considerably higher elution times, a new peak appeared, suggesting the formation of a low-molecular-weight by-product, which was attributed to adipic acid dihydrazide; nevertheless, its size was beyond the analytical range of SEC. These results strongly support the photo-induced cleavage of the acylhydrazone bonds along the main chain of the PEG-*alt*-AA alternating copolymer to produce the two precursor comonomers, PEG_{ald} and adipic acid dihydrazide.

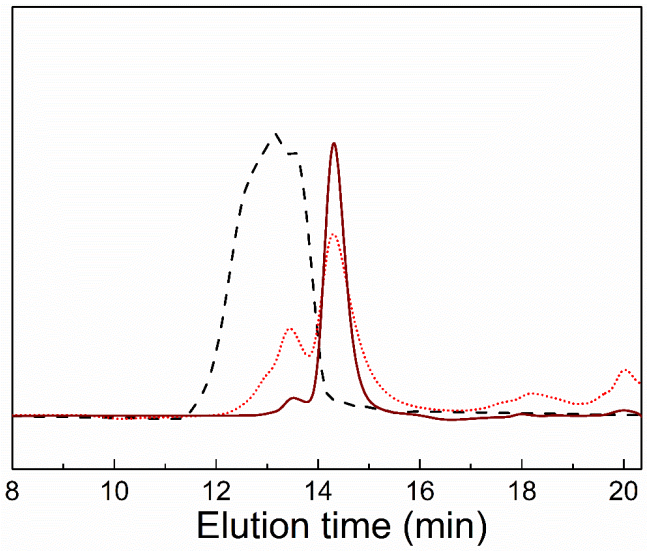

Figure 3.13. SEC traces of the PEG-*alt*-AA alternating copolymer (black dashed line), the PEG_{ald} precursor macromonomer (wine solid line) and the PEG-*alt*-AA copolymer after 1 h irradiation at 254 nm (red short dotted line).

3.5.2 Photodegradation of the PEG-*alt*-AA alternating copolymers monitored by UV-VIS spectroscopy.

UV-vis spectroscopy was used additionally to verify further the light-mediated breakdown of the acyhydrazone-based copolymer. The absorption spectra of a 0.2 mg ml^{-1} PEG-*alt*-AA copolymer solution in DMSO is shown in **Figure 3.14a**. Before irradiation, the polymer peak was centered at ~302 nm, whereas after exposure to UV light, the peak intensity progressively reduced and two new peaks at 260 nm and 288 nm emerged, which correlate to the absorption bands of the PEG_{ald} macromonomer, and support the SEC results discussed above. **Figure 3.14c** depicts the kinetics of the copolymer photodegradation process in DMSO, as assessed by the UV-vis spectra. An almost linear degradation profile was found for the first 60 min of irradiation, corresponding to ~55% cleavage of the polymer bonds, whereas for longer times the degradation kinetics were slowed down and reached 75% cleavage after 130 min irradiation.

Similar findings were obtained for the photodegradation process of the copolymer in water. Irradiation of an aqueous copolymer solution at pH 7.4, to avoid the acidic hydrolysis of the acylhydrazone bonds, resulted in the reduction of the absorbance at 302 nm, and simultaneously, to the appearance of a new peak at 260 nm, which corresponded to the PEG_{ald} macromonomer (**Figure 3.14b**). The rate of photodegradation in water was almost linear for more than 2 h irradiation time (**Figure 3.14d**), albeit significantly slower than that found in DMSO, with ~32% photocleavage occurring within the first 1 h of exposure. The lower accessibility of the hydrophobic aromatic acylhydrazone moieties to water molecules can be an assumption for the slower degradation rate in water.

It is worth noting, that despite the fact that the irradiation was carried out under UV illumination at 254 nm, which is considered as a harmful wavelength for biological applications, the irradiation dose used for the complete polymer degradation was extremely low (720 mJ cm^{-2}) when compared to other photodegradable polymers reported in the literature [78], [79].

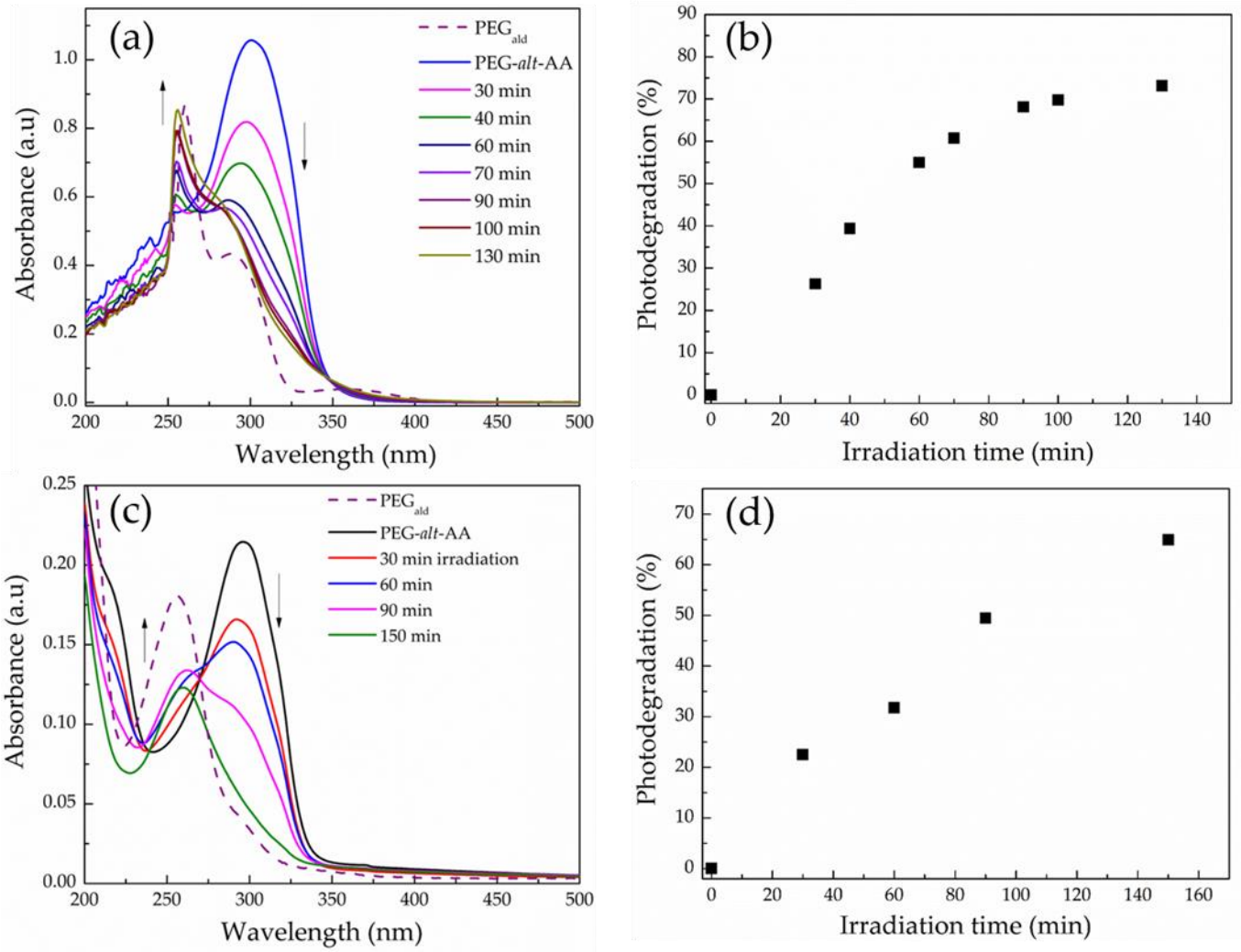

Figure 3.14. UV-vis absorption spectra of (a) a 0.2 mg ml^{-1} copolymer solution in DMSO and (b) a 0.02 mg ml^{-1} copolymer solution in H_2O at pH 7.4, upon irradiation at 254 nm. % photodegradation of the PEG-*alt*-AA copolymer as a function of irradiation time in (c) DMSO and (d) H_2O at pH 7.4.

3.6 Investigation of the dynamic nature of the acylhydrazone bonds following their photo-cleavage

As already discussed in Chapter 1.6.1, poly(acyl)hydrazones have been studied in the literature as dynamic covalent polymers, and have been proposed for the development of self-healing

materials and adaptable networks due to the reversible nature of the (acyl)hydrazone bonds, which can be cleaved and reformed in response to a stimulus, such as acidic media or temperature [59],[80],[81]. In order to investigate the dynamic nature of the acylhydrazone linkages of the PEG-*alt*-AA copolymers prepared in this work, a solution of the polymer in H_2O was first irradiated for 2 h at 254 nm to cleave the acylhydrazone bonds, and was then left under stirring for 24 h in the dark. The UV-vis absorption spectra of the copolymer after irradiation and following 24 h in the dark were compared (**Figure 3.15**), verifying that no changes in absorption took place in the dark, implying that the copolymer was not reformed.

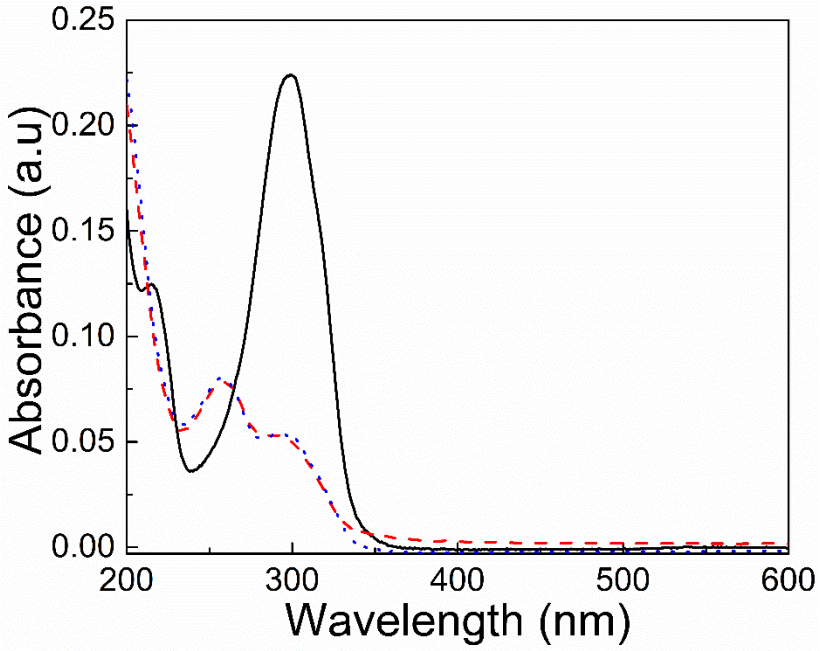

Figure 3.15. UV-vis absorption spectra of a 0.02 mgr ml^{-1} PEG-*alt*-AA alternating copolymer in H_2O before (black solid line) and after (red dashed line) irradiation for 2 h at 254 nm, and subsequently after stirring for 24 h in the dark (blue dotted line).

The sensitivity of the aldehyde groups generated at the PEG chain ends, following photocleavage of the acylhydrazone bonds by the light stimulus might explain this outcome. Aromatic and aliphatic aldehydes (or ketones) are well known to undergo a variety of photochemical reactions when exposed to UV light [82]. Light's interaction with aromatic aldehyde molecules, in particular, can result in the production of several radical species (**Scheme 3.4**).

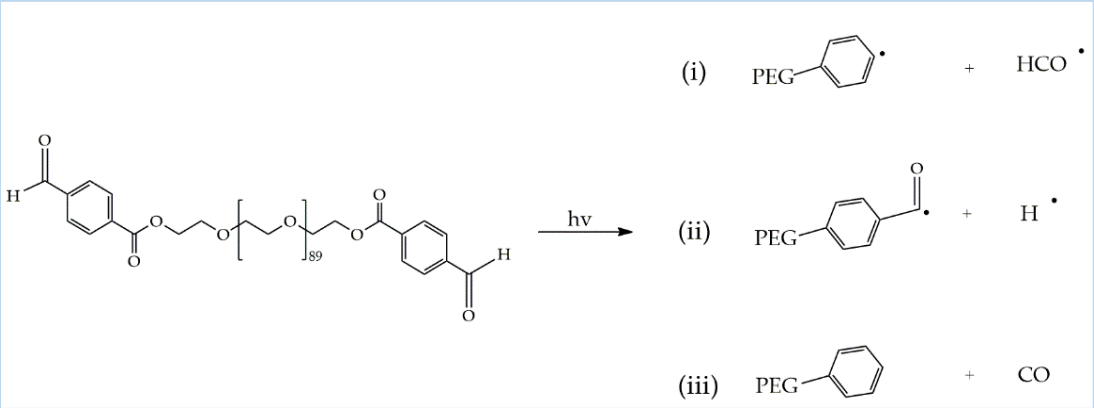

Scheme 3.4. Proposed photodissociation pathways of PEG_{ald} upon irradiation with UV light.

To further support our hypothesis, ^{1}H NMR spectroscopy was used to investigate the fate of the aldehyde end groups of PEG_{ald} after UV irradiation. **Figure 3.16** shows that the characteristic peak of the aldehyde protons at 10.11 ppm decreased significantly after 1 h of irradiation of the PEG_{ald} macromonomer at 254 nm, and disappeared completely after 2 h exposure to UV light. Moreover, the peaks attributed to the aromatic (7.99 and 8.24 ppm) and ester (4.53 ppm) protons changed and shifted to lower ppm, whereas two new peaks appeared at 2.2 ppm and 9.8 ppm, which were attributed to the formation of acetaldehyde as a by-product of the photodegradation reaction.

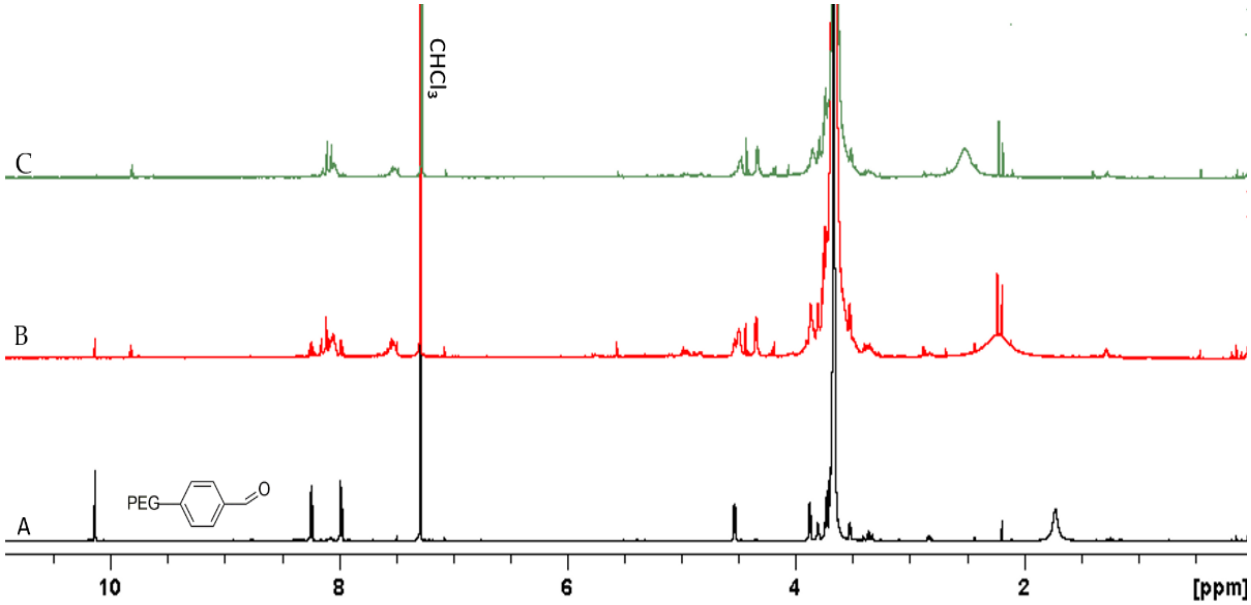

Figure 3.16. ^{1}H NMR spectra of PEG_{ald} (A) before, (B) after 1 h and (C) after 2 h irradiation at 254 nm in $CDCl_3$.

3.7 Synthesis of the PEG-*alt*-AA-DOX conjugates

The PEG-*alt*-AA alternating copolymer was used for the synthesis of the PEG-alt-AA-DOX drug conjugates. Before conjugation DOX·HCl was neutralized with TEA in DMSO in order to obtain the hydrophobic DOX molecules. For the conjugation of DOX at the ends of the poly-acylhydrazone chains, the copolymer and DOX were mixed at a 1:2 mole ratio in DMSO and were reacted for 24 h, followed by dialysis against DMSO in a dialysis bag with molecular weight cut off of 3500 kDa, to eliminate the unreacted DOX molecules. **Figure 3.17a** shows the UV-vis absorption spectrum of the PEG-*alt*-AA-DOX conjugate in DMSO, in which the polymer peak at 302 nm is clearly observed, whereas the inset shows the magnified spectrum in the 330–700 nm range, where the absorption peak of DOX is evident, indicating the successful conjugation of the drug at the polymer chain ends. **Figure 3.17b** shows the fluorescence emission spectra of the polymer, DOX and the PEG-*alt*-AA-DOX conjugate in DMSO. As expected, the copolymer does not emit light in the 500–800 nm range, whereas DOX and the PEG-*alt*-AA-DOX conjugate both emit at 600 nm, verifying the conjugation of the drug at the polymer chain ends. In addition, the slight shift of the fluorescent peak of the conjugates to higher wavelengths is a strong indication of the successful conjugation of the drug.

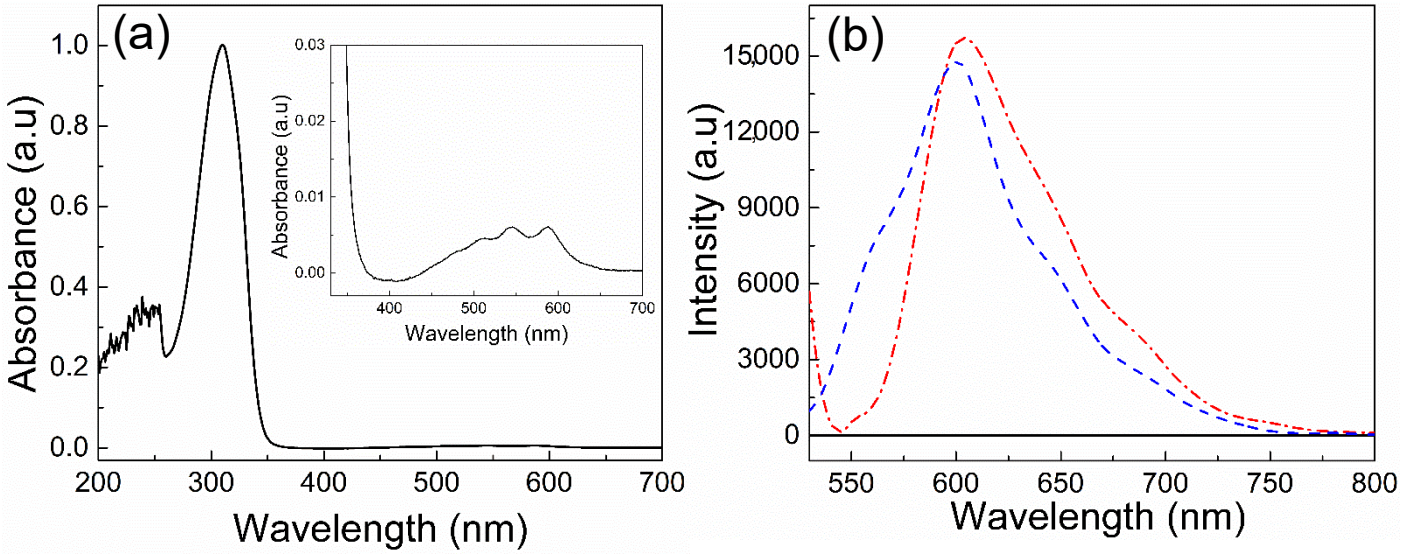

Figure 3.17. (a) UV-vis absorption spectrum of the PEG-*alt*-AA-DOX conjugate in DMSO (inset: magnified spectrum in the 340–700 nm range) and (b) fluorescence spectra of the PEG-*alt*-AA copolymer (black solid line), DOX (blue dashed line) and the PEG-*alt*-AA-DOX conjugate (red dashed dotted line).

In order to calculate the amount of conjugated DOX onto the PEG-*alt*-AA alternating copolymer a calibration curve was generated by measuring the fluorescent intensity of DOX solutions in DMSO at different drug concentrations (**Figure 3.18a**). The calibration curve is shown in **Figure 3.18b**. The drug binding onto the copolymer chains was calculated using equation 1 in Chapter 2.7 above and found 2.7 x 10^{-3} g DOX/g polymer. This result suggests a low drug binding onto the copolymer chains and explains the difficulty in observing the absorption band of DOX in the UV/Vis spectra of PEG-*alt*-AA-DOX conjugate.

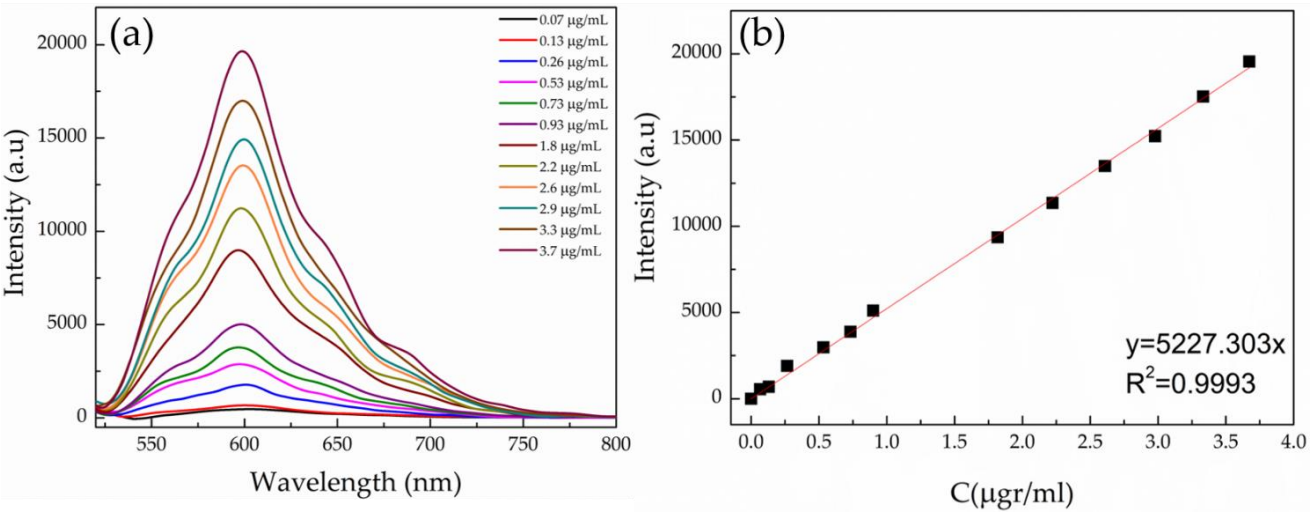

Figure 3.18. (a) Fluorescence emission spectra of DOX as a function of the drug concentration in DMSO and (b) standard calibration curve of DOX.

3.8. Self-Assembly of the PEG-*alt*-AA-DOX drug conjugates

As already discussed in Chapter 1.4.1, amphiphilic molecules containing a hydrophilic and a hydrophobic domain can self-assemble into various morphological structures (micelles, vesicles, cylinders, etc.) in water. We envisaged that the conjugation of the hydrophobic DOX moieties at one or both ends of the hydrophilic PEG-*alt*-AA copolymer chains, to produce amphiphilic drug conjugates, could drive their self-assembly into nanostructures with hydrophilic and hydrophobic compartments.

In order to test this hypothesis, the PEG-*alt*-AA-DOX conjugates were self-assembled in water using the dialysis method. First, the polymer-drug conjugates were dissolved in DMSO, which is considered as a good solvent for both the copolymer and the DOX drug, at a polymer concentration of 0.1g mL^{-1}, and next, an excess of neutral water (pH 7.4), to prevent the acidolysis

of the acylhydrazone bonds, was added dropwise to the organic solution, followed by the removal of DMSO by dialysis.

SEM and TEM were utilized to investigate the morphology of the PEG-*alt*-AA-DOX assemblies in water. Interestingly, spherical nanoparticles with an average diameter of ~300 nm were observed by SEM (**Figure 3.19a**), and a similar size (~300 nm) was found by TEM (**Figure 3.19b**). As described in the literature, carriers with a diameter on the order of 10 to 300 nm accumulate in cancerous tumors due to the enhanced permeability and retention (EPR) effect. It is noted that nanoparticles smaller than 10 nm are easily eliminated by renal clearance whereas, nanocarriers larger than 300 nm can be rapidly cleared from the bloodstream via the liver and spleen [83]. In comparison to the self-assembled polymer-drug conjugates described above, most of the polymeric self-assembled nanoparticles reported in the literature, comprise amphiphilic block copolymers, and have sizes between 10-300 nm, in which the hydrophobic block comprises the micellar core and the hydrophilic block forms the outer shell [84][85]. For instance, Fang –Yi Qiu et al. reported the preparation of redox-responsive polymer-drug conjugates composed of a PEG block and hydrophobic polyacrylate block, to which an anti-inflammatory drug was attached, to produce nanoparticles ~150-300 nm in diameter [86]. They also observed that as the length of the hydrophobic block was increased (resulting to the simultaneous increase of the molar feed ratio between the hydrophobic and the hydrophilic block), the diameter of the nanoparticles also increased. However, the self-assembly of single component polymer-drug conjugates has barely been investigated. Liu et al. conjugated docetaxel onto a medium molecular weight PEG (Mw > 2 kDa), generating spherical micelles ~46 nm in diameter [45].

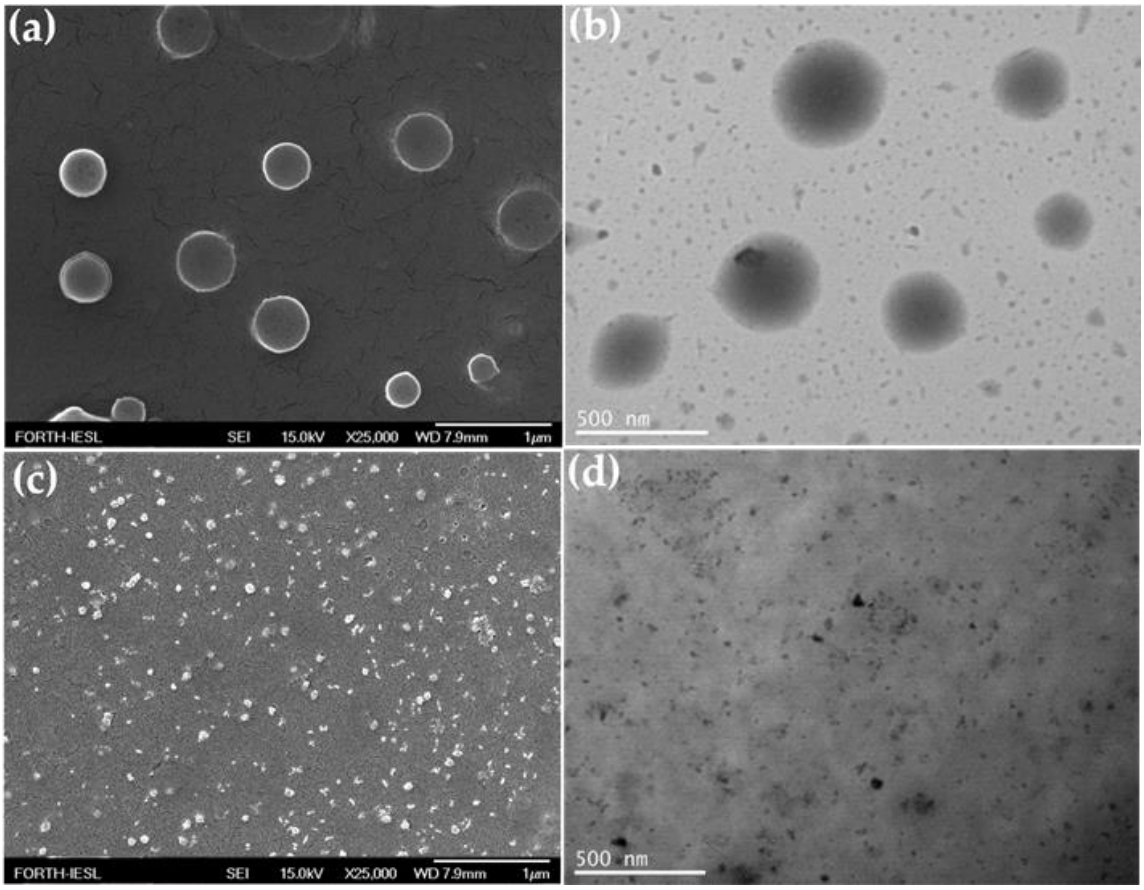

Figure 3.19. SEM (a and c) and TEM (b and d) images of the self-assembled PEG-*alt*-AA-DOX drug conjugates before (a and b) and after (c and d) irradiation for 2 h at 254 nm.

DLS measurements of the PEG-*alt*-AA-DOX assemblies were also carried out to support our findings from the electron microscopy experiments. The hydrodynamic size of the nanoparticles in water was found to be 250 nm **(Figure 3.20**), in good agreement with the SEM and TEM results discussed above.

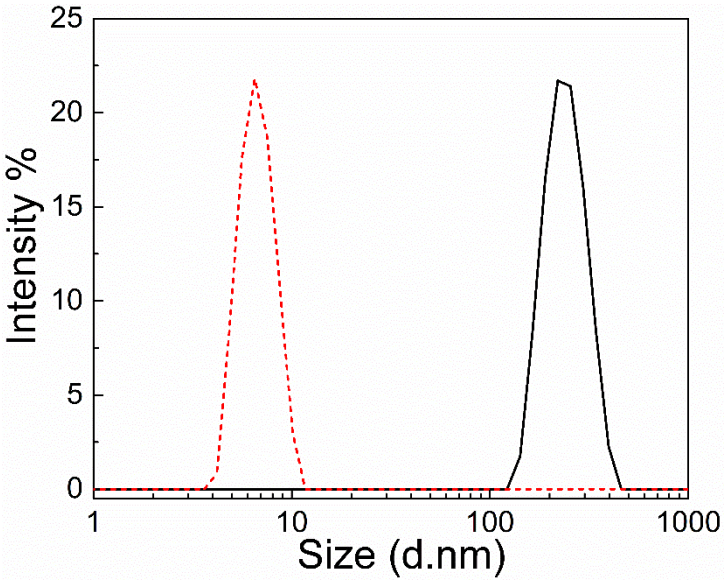

Figure 3.20. Hydrodynamic diameter for the PEG-*alt*-AA-DOX assemblies in water before (black solid line) and after (red dashed line) irradiation for 2 h at 254 nm.

3.9 Photo-induced degradation of the self-assembled PEG-*alt*-AA-DOX nanoparticles

Having established the photodegradation of the PEG-*alt*-AA copolymer (Chapter 3.4.2), the photo-mediated disruption of the self-assembled PEG-alt-AA-DOX nanoparticles upon the cleavage of the acylhydrazone bonds with UV light, was investigated by SEM, TEM and DLS. **Figure 3.19c** shows a SEM image of the self-assembled PEG-*alt*-AA-DOX conjugates in water (pH 7.4) following irradiation with UV light for 2 h. The absence of the PEG-*alt*-AA-DOX assemblies after irradiation is evident, indicating the main-chain cleavage of the polyacylhydrazone backbone. Indeed, smaller nanoparticles of size between 25–30 nm were observed in the SEM image after light irradiation, which can be attributed to aggregates formed by the released hydrophobic DOX molecules in water. These results were also confirmed by TEM (**Figure 3.19d**), which showed the absence of the spherical PEG-*alt*-AA-DOX assemblies observed before UV irradiation, and the presence of small, dark-colored nanoparticles (D ~ 15–20 nm) attributed to the released drug aggregates. Finally, the disruption of the self-assembled PEG-*alt*-AA-DOX nanostructures, upon exposure to UV light, was verified by DLS (**Figure 3.20**). The large particles disappeared and a hydrodynamic diameter of ~6.5 nm was measured, which was attributed to the constituent PEG macromonomer chains that remained in the solution after

the degradation of the polymer backbone. These results also confirm the complete disruption of the PEG-*alt*-AA-DOX assemblies after 2 h UV irradiation.

3.10. Photo- and acid-induced disruption of the self-assembled PEG-*alt*-AA-DOX nanoparticles and release of the drug

Stimuli-controlled drug release from polymeric nanocarriers has attracted significant interest over the past decades. As discussed in Chapter 1.6.2 above, light offers remarkable advantages as an external stimulus, such as spatiotemporal control, as well as tunability of the irradiation wavelength and intensity while it is often inexpensive. After the study of the photo-induced degradation of the PEG-*alt*-AA-DOX assemblies, the synergistic effect of light and acidic pH on their disruption was investigated. As discussed previously the acylhydrazone bonds are acid-labile, which renders them relevant materials for drug release in a cancer microenvironment that is slightly acidic. For this, two aqueous solutions of the PEG-*alt*-AA-DOX assemblies with adjusted pH values at 7.4 and 5.2, respectively, were prepared and their photo-induced disruption was investigated by UV-Vis spectroscopy. **Figure 3.21a** shows the UV-vis absorption spectra of the aqueous PEG-*alt*-AA-DOX solution at pH 7.4, for different irradiation times at 254 nm (0.1 mW cm^{-2}). As discussed above, the characteristic absorption band of the polymer at ~302 nm decreased with the irradiation time, while a new band at ~260 nm emerged, indicating the main-chain cleavage of the polymer backbone and the formation of the precursor PEG macromonomer. A similar degradation process was found for the PEG-*alt*-AA-DOX assemblies upon the irradiation of the polymer solution adjusted to pH 5.2 (**Figure 3.21b**), whilst, when comparing the degradation rates at the two pH values, a slightly faster degradation of the polymer—and thus disruption of the assemblies—was found at the low solution pH. In particular, 75% of the polymer was cleaved after 2 h irradiation at pH 7.4, whereas the degree of degradation reached 90% for the same irradiation time at pH 5.2 (**Figure 3.21c**), suggesting the synergistic photo- and acidolysis of the labile bonds of the polymer.

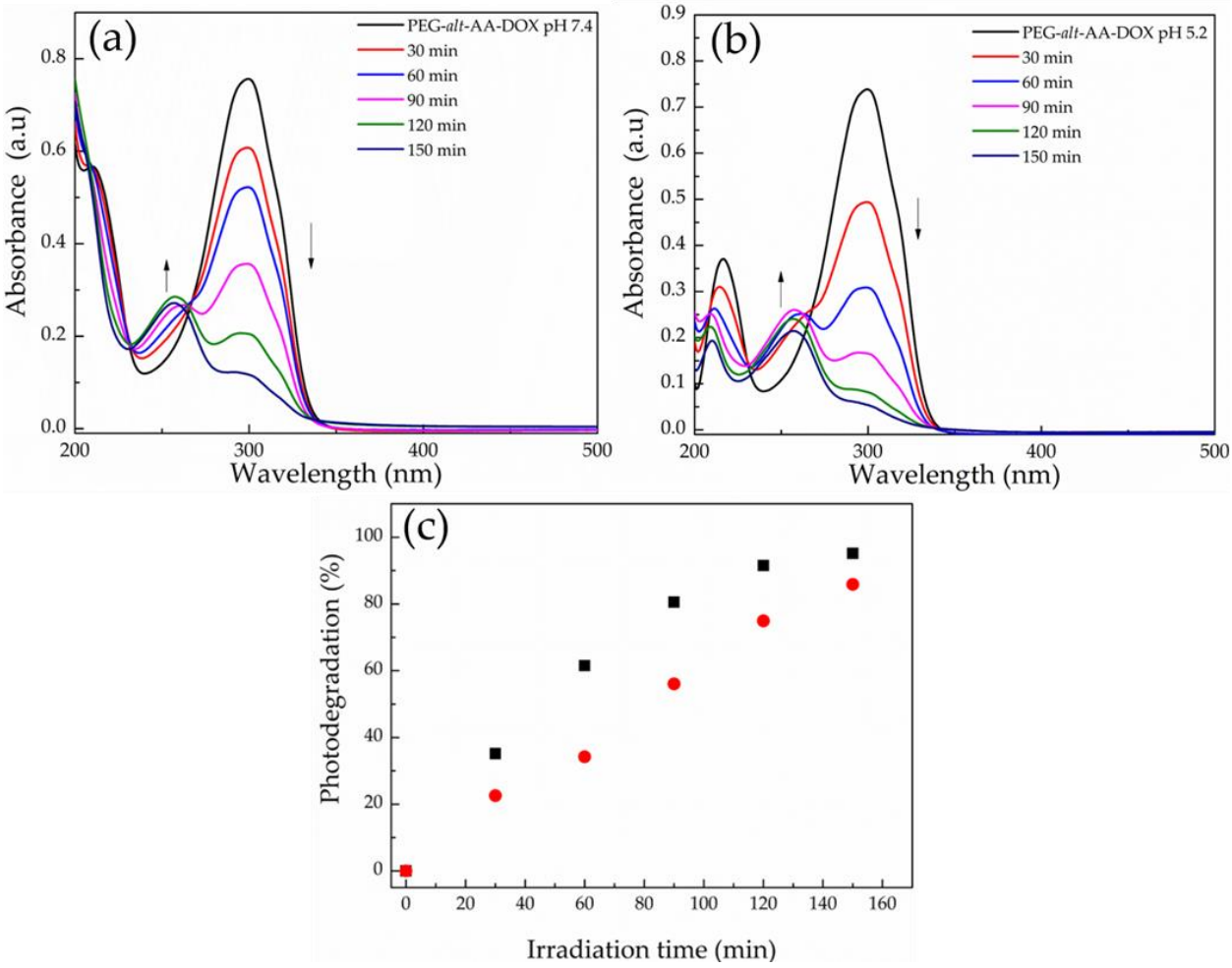

Figure 3.21. UV-Vis absorption spectra of an aqueous PEG-*alt*-AA-DOX solution at (a) pH 7.4 and (b) pH 5.2 for different irradiation intervals at 254 nm. (c) The photodegradation percentage of the PEG-*alt*-AA-DOX nanoparticles as a function of irradiation time at pH 7.4 (red dots) and pH 5.2 (black squares).

It should be noted that the low DOX content of the PEG-*alt*-AA-DOX assemblies prohibited the quantification of the photo-induced drug release by UV-vis spectroscopy. Therefore, fluorescence spectroscopy was used instead to quantify the drug release profile.

For this, an aqueous PEG-*alt*-AA-DOX solution was first adjusted to pH 5.2 to simulate the acidic environment of a tumor tissue, and was next irradiated with UV light for different irradiation intervals, up to 2 h total irradiation time. The solution was dialyzed against water (pH 5.2) during the irradiation; the dialysate was collected after each irradiation cycle, and its DOX content was

analyzed by fluorescence spectroscopy. In parallel, another PEG-*alt*-AA-DOX solution at neutral pH 7.4 was irradiated with UV light, and the release of the cargo in the dialysate was followed by fluorescence spectroscopy. As shown in **Figure 3.22**, the release kinetics of the conjugated DOX molecules upon irradiation at pH 5.2 and pH 7.4 were similar (60–65% released DOX at 2 h), denoting that the release of the drug is dominated by the photoinduced cleavage of the acylhydrazone bonds, whereas the solution pH, in this range, does not play a significant role in the drug release profile at short irradiation times (2 h). This outcome supports the results discussed in Chapter 3.5, in which the degradation profile of the PEG-*alt*-AA copolymer was found to be rather low at pH 5.2 in the first 2 h (**Figure 3.10**) and became significant only after 23 h in this pH value. The slow acidolysis of the hydrazone bonds and the low amount of released cargo at pH 5.0 and 5.5 has been previously reported in the literature [36], [87], [88].

In order to increase the release kinetics of the DOX molecules from the PEG-*alt*-AA-DOX assemblies, an aqueous PEG-*alt*-AA-DOX solution at pH 2.0 was irradiated with UV light for 2 h. Indeed, a faster drug release profile was found (**Figure 3.22**, black squares), with 64% of the DOX being released after 1 h irradiation and, reaching 82% free drug at 2 h. On the contrary, the solution pH alone (pH 2 without light irradiation) resulted in only 35% drug release in 2 h (red circles).

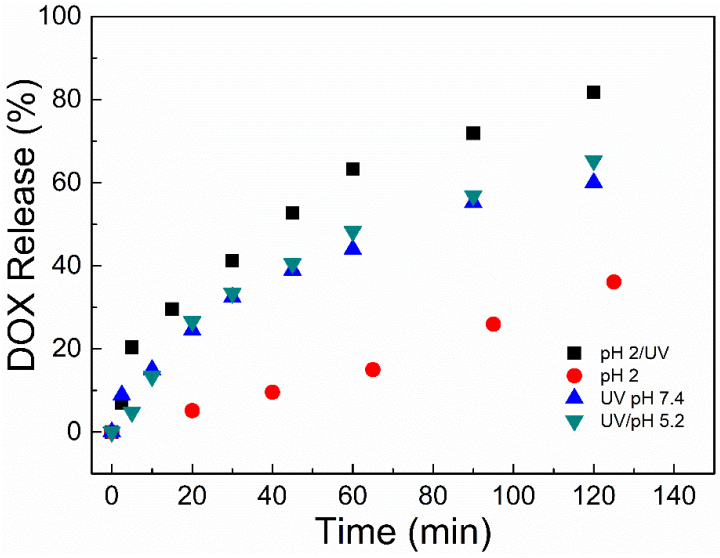

Figure 3.22. Time-dependant release profile of DOX from the PEG-*alt*-AA-DOX assemblies upon irradiation (254 nm, 0.1 mW cm^{-2}) at pH 7.4 (blue triangles), pH 5.2 (green triangles) and pH 2 (red squares), and the control sample (without irradiation) at pH 2 (black circles).

Based on the above results, light irradiation is a convenient and remote stimulus, allowing to control the drug release from the PEG-*alt*-AA-DOX assemblies in short times, whereas the solution pH enables the prolonged release of the cargo. As it can be seen in Figure 3.22 the low acidic pH (pH 2) alone, exhibits a low rate of DOX release, compared to UV light irradiation at neutral or mildly acidic environment that demonstrates a faster release. Finally, the synergistic photolysis and acidolysis of the polymer prodrug upon irradiation at very low pH values (pH 2.0), leads to faster release kinetics. Therefore, the proposed drug delivery system could be used for the effective photo-triggered drug release at specific sites/tissues, in which the pH ranges from neutral (normal tissues) to acidic (cancer tissues), providing an additional level of control over the drug release profile.

Chapter 4

Conclusions and Future Perspectives

Cancer is one of the most serious health issues currently in developed countries and it is the result of deregulation of the mechanisms that control the behavior of normal cells. Despite countless advances in cancer medicine, cancer treatment is still a huge challenge. Among them, chemotherapy is a commonly used treatment, which involves the administration of therapeutic drugs directly into the bloodstream. The main flaw of chemotherapy in the treatment of cancer is its inability to distinguish between cancerous and non-cancerous cells. The effectiveness of cancer chemotherapy is restricted due to its low adsorption by cancer cells and its significant damage to normal cells. Furthermore, most anti-cancer medicines are not water soluble, resulting in low cellular absorption. There are many drug delivery systems under development, other in clinical trials and other under preliminary investigation with promising results, whereas some are being utilized in accordance with the FDA regulation, all aiming to overcome the drawbacks of chemotherapy. The future may hold a drug delivery system for every cancer, perhaps as a hybrid formulation combining multiple carrier types carrying a cocktail of chemo- and immunotherapeutic drugs for highly personalized therapy.

The aim of this master thesis was to propose a new, main-chain photo- and acid-degradable, amphiphilic polymer–drug conjugate, based on a hydrophilic polyacylhydrazone chain and a hydrophobic model anticancer drug, DOX. The alternating polyacylhydrazone copolymer was synthesized via a step-growth polymerization reaction of adipic acid dihydrazide with dibenzaldehyde-terminated PEG. At first, the acidic hydrolysis of the copolymer at pH 5.2 (in order to simulate the pH values of cancer tissues) was studied, and the degradation of the PEG-*alt*-AA copolymer was observed only after 5 days exposure to this pH stimulus. The photodegradation profile of the PEG-*alt*-AA copolymer in DMSO and water, upon irradiation at 254 nm (0.1 mW cm^{-2}), was studied, and the cleavage of the hydrazone bonds along the polymer main-chain, to produce the two precursor comonomers, was verified at very low irradiation doses (720 mJ/cm^{-1}). Next, amphiphilic PEG-*alt*-AA-DOX conjugates were prepared by the condensation of DOX molecules at the polymer chain end(s), and the conjugates were self-assembled in water to form spherical nanoparticles. At neutral and slightly acidic pH values (pH 5.2), the PEG-*alt*-AA-DOX assemblies were disrupted, and the conjugated drug was released at short irradiation times and a low total irradiation dose, whereas the drug-release kinetics were accelerated upon the

synergistic effect of light irradiation and a low solution pH (2.0), denoting the remotely controlled drug release.

Based on the results discussed above, we envisage that such photo- and acid-degradable polymers could be used for the conjugation and controlled delivery of both hydrophilic and hydrophobic drug molecules, vitamins or other bioactive molecules bearing an aldehyde or ketone group, and are thus attractive for the development of diverse drug carriers.

The primary concern in future prospects of this master thesis should be, on the one hand, the investigation of the biocompatibility of the PEG-alt-AA alternating copolymer and on the other hand, the examination of the effectiveness of the polymer–drug conjugates in killing cancer cells. In addition, the drug loading capacity of the synthesized copolymer should be further examined, as the DOX concentration conjugated to the PEG-*alt*-AA copolymer was found to be quite low (2.7×10^{-3} g DOX/g polymer), compared to other polymer-drug conjugates. A higher percentage of conjugated DOX could be also accomplished by modifying the polymer in order to conjugate the drug onto the polymer side groups in addition to the polymer chain ends. Lastly, the self-assembly of the PEG-alt-AA-DOX conjugates, should be further investigated, as poly(acyl)hydrazones have been reported to undergo extensive hydrogen bonding interactions between the polymer chains (see discussion in Chapter 1.6.1). The role and strength of these interactions in the self-assembly of the PEG-*alt*-AA-DOX conjugates should be examined.

Furthermore, as already discussed above, the photo-induced disruption of the PEG-*alt*-AA-DOX assemblies and the release of DOX were carried out upon UV irradiation at 254 nm, which is considered a harmful wavelength for biological applications, and despite the very low irradiation dose used for the complete polymer degradation (720 mJ cm^{-2}), further research should be carried out aiming to red-shift the irradiation wavelength required for the photodegradation of the polymer acylhydrazone bonds and therefore improve their potential in the biomedical field.

Finally, in this project the synergistic effect of light and the solution pH on the disruption of the PEG-alt-AA-DOX assemblies, was investigated. In future work, different stimuli can be combined with light in order to achieve better spatiotemporal control and more effective release of the therapeutic cargo. For example, the cleavage of the acylhydrazone bonds of the PEG-alt-AA alternating copolymer can be examined upon application of various stimuli, such as the solution temperature and ultrasound. Lastly, to address a more effective tumor targeting, the polymer-drug conjugates synthesized in this thesis can be additionally decorated with cancer cell recognition moieties, such as antibodies or their receptors, to target specific diseased tissues.

References

[1] H. Sung *et al.*, “Global Cancer Statistics 2020 : GLOBOCAN Estimates of Incidence and Mortality Worldwide for 36 Cancers in 185 Countries,” vol. 71, no. 3, pp. 209–249, 2021, doi: 10.3322/caac.21660.

[2] J. Ferlay *et al.*, “Cancer statistics for the year 2020 : An overview,” no. February, pp. 778–789, 2021, doi: 10.1002/ijc.33588.

[3] K. J. Harrington, “Biology of cancer.”

[4] R. R. Seeley, P. Tate, and T. D. Stephens, *Anatomia & Fisiologia*. 2005.

[5] D. Hanahan and R. A. Weinberg, “Hallmarks of cancer: The next generation,” *Cell*, vol. 144, no. 5, pp. 646–674, 2011, doi: 10.1016/j.cell.2011.02.013.

[6] K. Park and A. E. Dream, *Cancer Targeted Drug Delivery*. 2013.

[7] P. EHRLICH, “Partial Cell Functions,” *Scand. J. Immunol.*, vol. 31, no. 1, pp. 4–13, 1990, doi: 10.1111/j.1365-3083.1990.tb02737.x.

[8] K. K. Jain, “Advances in the field of nanooncology,” *BMC Med.*, vol. 8, p. 83, 2010, doi: 10.1186/1741-7015-8-83.

[9] S. Senapati, A. K. Mahanta, S. Kumar, and P. Maiti, “Controlled drug delivery vehicles for cancer treatment and their performance,” *Signal Transduct. Target. Ther.*, vol. 3, no. 1, pp. 1–19, 2018, doi: 10.1038/s41392-017-0004-3.

[10] S. Hossen, M. K. Hossain, M. K. Basher, M. N. H. Mia, M. T. Rahman, and M. J. Uddin, “Smart nanocarrier-based drug delivery systems for cancer therapy and toxicity studies: A review,” *J. Adv. Res.*, vol. 15, pp. 1–18, 2019, doi: 10.1016/j.jare.2018.06.005.

[11] F. Danhier, O. Feron, and V. Préat, “To exploit the tumor microenvironment: Passive and active tumor targeting of nanocarriers for anti-cancer drug delivery,” *J. Control. Release*, vol. 148, no. 2, pp. 135–146, 2010, doi: 10.1016/j.jconrel.2010.08.027.

[12] J. A. Nagy, A. M. Dvorak, and H. F. Dvorak, “Vascular hyperpermeability, angiogenesis, and stroma generation,” *Cold Spring Harb. Perspect. Med.*, vol. 2, no. 2, pp. 1–14, 2012, doi: 10.1101/cshperspect.a006544.

[13] Y. Matsumura and H. Maeda, “A New Concept for Macromolecular Therapeutics in Cancer Chemotherapy: Mechanism of Tumoritropic Accumulation of Proteins and the Antitumor Agent Smancs,” *Cancer Res.*, vol. 46, no. 8, pp. 6387–6392, 1986.

[14] V. Torchilin, “Tumor delivery of macromolecular drugs based on the EPR effect,” *Adv. Drug Deliv. Rev.*, vol. 63, no. 3, pp. 131–135, 2011, doi: 10.1016/j.addr.2010.03.011.

[15] J. W. Nichols and Y. H. Bae, “EPR: Evidence and fallacy,” *J. Control. Release*, vol. 190, pp. 451–464, 2014, doi: 10.1016/j.jconrel.2014.03.057.

[16] F. Danhier, “To exploit the tumor microenvironment: Since the EPR effect fails in the clinic, what is the future of nanomedicine?,” *J. Control. Release*, vol. 244, pp. 108–121, 2016, doi: 10.1016/j.jconrel.2016.11.015.

[17] T. Lammers, F. Kiessling, W. E. Hennink, and G. Storm, “Drug targeting to tumors:

Principles, pitfalls and (pre-) clinical progress," *J. Control. Release*, vol. 161, no. 2, pp. 175–187, 2012, doi: 10.1016/j.jconrel.2011.09.063.

[18] J. Sato, W. van Osdol, J. N. Weinstein, and M. J. Perez-Bacete, "Micropharmacology of Monoclonal Antibodies in Solid Tumors: Direct Experimental Evidence for a Binding Site Barrier," *Cancer Res.*, vol. 52, no. 19, pp. 5144–5153, 1992.

[19] M. C. Scicluna and L. Vella-zarb, "Evolution of Nanocarrier Drug-Delivery Systems and Recent Advancements in Covalent Organic Framework − Drug Systems," 2020, doi: 10.1021/acsanm.9b02603.

[20] S. Chen *et al.*, "Inorganic Nanomaterials as Carriers for Drug Delivery," vol. 12, no. 1, pp. 1–27, 2016, doi: 10.1166/jbn.2016.2122.

[21] A. I. Journal, J. Xu, K. Liao, H. Jiang, and W. Zhou, "Research progress of novel inorganic nanometre materials carriers in nanomedicine for cancer diagnosis and treatment," *Artif. Cells, Nanomedicine, Biotechnol.*, vol. 0, no. 0, pp. 1–11, 2018, doi: 10.1080/21691401.2018.1499665.

[22] H. Huang, W. Feng, Y. Chen, and J. Shi, "Nano Today Inorganic nanoparticles in clinical trials and translations," *Nano Today*, vol. 35, p. 100972, 2020, doi: 10.1016/j.nantod.2020.100972.

[23] A. R. Rastinehad, H. Anastos, E. Wajswol, J. S. Winoker, J. P. Sfakianos, and S. K. Doppalapudi, "Gold nanoshell-localized photothermal ablation of prostate tumors in a clinical pilot device study," 2019, doi: 10.1073/pnas.1906929116.

[24] J. J. Lee and C. A. Che, "A review on current nanomaterials and their drug conjugate for targeted breast cancer treatment," pp. 2373–2384, 2017.

[25] A. M. Seifalian and M. Loizidou, "Organic nanocarriers for cancer drug delivery ´ vila , Alexander M Seifalian and Marilena Loizidou ´ ctor Lo," no. Figure 1, 2012, doi: 10.1016/j.coph.2012.02.011.

[26] D. A. Dri, C. Marianecci, M. Carafa, E. Gaucci, and D. Gramaglia, "Surfactants , Nanomedicines and Nanocarriers : A Critical Evaluation on Clinical Trials," pp. 1–21, 2021.

[27] A. Z. Wang, R. Langer, and O. C. Farokhzad, "Nanoparticle Delivery of Cancer Drugs," 2012, doi: 10.1146/annurev-med-040210-162544.

[28] V. P. Torchilin, "RECENT ADVANCES WITH LIPOSOMES AS PHARMACEUTICAL CARRIERS," vol. 4, no. February, 2005, doi: 10.1038/nrd1632.

[29] N. K. Verma, G. Alam, and J. N. Mishra, "A Review of Dendrimer-based Approach to Novel Drug Delivery Systems A Review of Dendrimer-based Approach to Novel Drug Delivery Systems," no. September 2016, 2015, doi: 10.37285/ijpsn.2015.8.3.3.

[30] Y. Zhang, Y. Huang, and S. Li, "Polymeric Micelles : Nanocarriers for Cancer-Targeted Drug Delivery," 2014, doi: 10.1208/s12249-014-0113-z.

[31] D. E. Discher and F. Ahmed, "Polymersomes," 2006, doi: 10.1146/annurev.bioeng.8.061505.095838.

[32] S. Wadhwa and R. J. Mumper, "Polymer-Drug Conjugates for Anticancer Drug Delivery," vol. 32, no. 3, pp. 215–245, 2015.

[33] J. Hyung, G. Saravanakumar, K. Kim, and I. Chan, "Targeted delivery of low molecular

drugs using chitosan and its derivatives ☆," *Adv. Drug Deliv. Rev.*, vol. 62, no. 1, pp. 28–41, 2010, doi: 10.1016/j.addr.2009.10.003.

[34] R. Duncan, "Soluble Synthetic Polymers as Potential Drug Carriers," 1984.

[35] X. Pang, H. Du, H. Zhang, Y. Zhai, and G. Zhai, "Polymer – drug conjugates : present state of play and future perspectives," *Drug Discov. Today*, vol. 18, no. 23–24, pp. 1316–1322, 2018, doi: 10.1016/j.drudis.2013.09.007.

[36] S. Dong *et al.*, "Multifunctional Polymeric Prodrug with Simultaneous Conjugating Camptothecin and Doxorubicin for pH/Reduction Dual-Responsive Drug Delivery," *ACS Appl. Mater. Interfaces*, vol. 11, pp. 8740–8748, 2019, doi: 10.1021/acsami.8b16363.

[37] S. Downstate, "Enzyme- and pH-sensitive Branched Polymer- Doxorubicin Conjugate-Based Nanoscale Drug Delivery System for Cancer Therapy," 2016, doi: 10.1021/acsami.6b02006.

[38] Y. Zhang, Q. Yin, L. Yin, L. Ma, L. Tang, and J. Cheng, "Chain-Shattering Polymeric Therapeutics with On-Demand Drug-Release Capability ** Angewandte," pp. 6435–6439, 2013, doi: 10.1002/anie.201300497.

[39] C. Biology, O. Street, C. Engineering, and S. G. Street, "Using shape for self-assembly," pp. 2824–2847, 2012, doi: 10.1098/rsta.2011.0254.

[40] B. Parshad, S. Prasad, S. Bhatia, A. Mittal, and Y. Pan, "Non-ionic small amphiphile based nanostructures for biomedical applications," pp. 42098–42115, 2020, doi: 10.1039/d0ra08092f.

[41] C. Avogadro, *No Title*. .

[42] K. E. B. Doncom, L. D. Blackman, D. B. Wright, and M. I. Gibson, "Europe PMC Funders Group Dispersity Effects in Polymer Self-Assemblies : A Matter of Hierarchical Control," vol. 46, no. 14, pp. 4119–4134, 2018, doi: 10.1039/c6cs00818f.Dispersity.

[43] R. Duncan, P. Kopeckov, J. B. Lloyd, J. Kopecek, H. C. Cable, and J. Pohl, "Anticancer agents coupled to N- (2-hydroxypropyl) methacrylamide copolymers . I . Evaluation of daunomycin and puromycin conjugates in vitro," vol. 174, pp. 165–174, 1987.

[44] M. Yokoyama, M. Miyauchi, N. Yamada, T. Okano, Y. Sakurai, and K. Kataoka, "Characterization and Anticancer Activity of the Micelle-forming Polymeric Anticancer Drug Adriamycin-conjugated Poly (ethylene glycol) -Poly (aspartic acid) Block Copolymer," no. 1, pp. 1693–1700, 1990.

[45] J. Liu, P. Zahedi, F. Zeng, and C. Allen, "Nano-Sized Assemblies of a PEG-Docetaxel Conjugate as a Formulation Strategy for Docetaxel," vol. 97, no. 8, pp. 3274–3290, 2008, doi: 10.1002/jps.

[46] T. Manouras and M. Vamvakaki, "Polymer Chemistry," pp. 74–96, 2017, doi: 10.1039/c6py01455k.

[47] D. Schmaljohann, "Thermo- and pH-responsive polymers in drug delivery ☆," vol. 58, pp. 1655–1670, 2006, doi: 10.1016/j.addr.2006.09.020.

[48] H. P. James, R. John, A. Alex, and K. R. Anoop, "Smart polymers for the controlled delivery of drugs – a concise overview," vol. 4, no. 2, pp. 120–127, 2014, doi: 10.1016/j.apsb.2014.02.005.

[49] J. R. Casey, S. Grinstein, and J. Orlowski, “Sensors and regulators of intracellular pH,” *Nat. Rev. Mol. Cell Biol.*, vol. 11, no. 1, pp. 50–61, 2009, doi: 10.1038/nrm2820.

[50] M. Karimi *et al.*, *Chem Soc Rev*. Royal Society of Chemistry, 2016.

[51] Y. Liu, W. Wang, J. Yang, C. Zhou, and J. Sun, “pH-sensitive polymeric micelles triggered drug release for extracellular and intracellular drug targeting delivery,” *Asian J. Pharm. Sci.*, 2013, doi: 10.1016/j.ajps.2013.07.021.

[52] Q. Zha *et al.*, “Acid – degradable carboxymethyl chitosan nanogels via an ortho ester linkage mediated improved penetration and growth inhibition of 3-D tumor spheroids in vitro,” *Mater. Sci. Eng. C*, vol. 78, pp. 246–257, 2017, doi: 10.1016/j.msec.2017.04.098.

[53] B. Liu and S. Thayumanavan, “Substituent Effects on the pH Sensitivity of Acetals and Ketals and Their Correlation with Encapsulation Stability in Polymeric Nanogels Substituent Effects on the pH Sensitivity of Acetals and Ketals and Their Correlation with Encapsulation Stability in ,” 2017, doi: 10.1021/jacs.6b11181.

[54] S. J. Sonawane, R. S. Kalhapure, and T. Govender, “European Journal of Pharmaceutical Sciences Hydrazone linkages in pH responsive drug delivery systems,” *Eur. J. Pharm. Sci.*, vol. 99, pp. 45–65, 2017, doi: 10.1016/j.ejps.2016.12.011.

[55] A. Mihaela, L. Mititelu, M. Pinteala, and L. Marin, “Journal of Colloid and Interface Science Nitrosalicyl-imine-chitosan hydrogels based drug delivery systems for long term sustained release in local therapy,” *J. Colloid Interface Sci.*, vol. 536, pp. 196–207, 2019, doi: 10.1016/j.jcis.2018.10.048.

[56] R. Article, “Chem Soc Rev and sensors,” 2014, doi: 10.1039/c3cs60385g.

[57] T. Yoshida, T. C. Lai, G. S. Kwon, and K. Sako, “pH- and ion-sensitive polymers for drug delivery,” pp. 1–17, 2013.

[58] R. S. Greenfield *et al.*, “Evaluation in Vitro of Adriamycin Immunoconjugates Synthesized Using an Acid-sensitive Hydrazone Linker,” vol. 5, no. 19, pp. 6600–6608, 1990.

[59] N. Kuhl *et al.*, “Acylhydrazones as Reversible Covalent Crosslinkers for Self-Healing Polymers,” pp. 3295–3301, 2015, doi: 10.1002/adfm.201501117.

[60] P. Chakma and D. Konkolewicz, “Dynamic Covalent Bonds in Polymeric Materials,” *Angew. Chemie*, vol. 131, no. 29, pp. 9784–9797, 2019, doi: 10.1002/ange.201813525.

[61] J. M. Winne, L. Leibler, and F. E. Du Prez, “Dynamic covalent chemistry in polymer networks: A mechanistic perspective,” *Polym. Chem.*, vol. 10, no. 45, pp. 6091–6108, 2019, doi: 10.1039/c9py01260e.

[62] G. Deng, C. Tang, F. Li, H. Jiang, and Y. Chen, “Covalent cross-linked polymer gels with reversible sol-gel transition and self-healing properties,” *Macromolecules*, vol. 43, no. 3, pp. 1191–1194, 2010, doi: 10.1021/ma9022197.

[63] W. G. Skene and J. M. P. Lehn, “Dynamers: Polyacylhydrazone reversible covalent polymers, component exchange, and constitutional diversity,” *Proc. Natl. Acad. Sci. U. S. A.*, vol. 101, no. 22, pp. 8270–8275, 2004, doi: 10.1073/pnas.0401885101.

[64] R. H. Michel and W. A. Murphey, “Polymers from the condensation of dihydrazides with dialdehydes and diketones,” *J. Appl. Polym. Sci.*, vol. 7, no. 2, pp. 617–624, 1963, doi: 10.1002/app.1963.070070218.

[65] C. Brieke, F. Rohrbach, A. Gottschalk, G. Mayer, and A. Heckel, “Light-Controlled Tools Angewandte,” pp. 2–33, 2012, doi: 10.1002/anie.201202134.

[66] T. Manouras and M. Vamvakaki, “Field responsive materials: photo-, electro-, magnetic- and ultrasound-sensitive polymers,” *Polym. Chem.*, vol. 8, no. 1, pp. 74–96, 2017, doi: 10.1039/C6PY01455K.

[67] G. Pasparakis, T. Manouras, P. Argitis, and M. Vamvakaki, “Photodegradable polymers for biotechnological applications,” *Macromol. Rapid Commun.*, vol. 33, no. 3, pp. 183–198, 2012, doi: 10.1002/marc.201100637.

[68] G. Pasparakis, T. Manouras, A. Selimis, and M. Vamvakaki, “Laser-Induced Cell Detachment and Patterning with Photodegradable Polymer Substrates **,” no. Scheme 1, pp. 4142–4145, 2011, doi: 10.1002/anie.201007310.

[69] G. Pasparakis, T. Manouras, M. Vamvakaki, and P. Argitis, “Harnessing photochemical internalization with dual degradable nanoparticles for combinatorial photo-chemotherapy,” *Nat. Commun.*, vol. 5, p. 3623, 2014, doi: 10.1038/ncomms4623.

[70] A. Manuscript, “ChemComm,” 2021, doi: 10.1039/D1CC00124H.

[71] M. Psarrou, M. G. Kothri, M. Vamvakaki, H. Anastasiadis, and H. Iatrou, “Photo-and Acid-Degradable Polyacylhydrazone-Doxorubicin Conjugates,” 2021, doi: 10.3390/polym13152461.

[72] Y. Zhang, L. Tao, S. Li, and Y. Wei, “Synthesis of multiresponsive and dynamic chitosan-based hydrogels for controlled release of bioactive molecules,” *Biomacromolecules*, vol. 12, no. 8, pp. 2894–2901, 2011, doi: 10.1021/bm200423f.

[73] B. W. Chieng, N. A. Ibrahim, W. Zin, W. Yunus, and M. Z. Hussein, “Poly(lactic acid)/Poly(ethylene glycol) Polymer Nanocomposites: Effects of Graphene Nanoplatelets,” no. December, 2013, doi: 10.3390/polym6010093.

[74] R. Nguyen, I. Huc, I. Européen, D. Chimie, A. P. Berland, and P. Cedex, “Optimizing the reversibility of hydrazone formation for dynamic combinatorial chemistry groups , and aromatic or aliphatic aldehydes form and,” pp. 2–3, 2003.

[75] D. K. Ko and E. T. Kool, “Oximes and Hydrazones in Bioconjugation : Mechanism and Catalysis,” 2017, doi: 10.1021/acs.chemrev.7b00090.

[76] A. John Maria Xavier, M. Thakur, and J. Margaret Marie, “Synthesis and spectral characterisation of hydrazone based 14-membered octaaza macrocyclic Ni(II) complexes,” *J. Chem. Pharm. Res.*, vol. 4, no. 2, pp. 986–990, 2012.

[77] A. A. Kale and V. P. Torchilin, “Design , Synthesis , and Characterization of pH-Sensitive PEG - PE Conjugates for Stimuli-Sensitive Pharmaceutical Nanocarriers : The Effect of Substitutes at the Hydrazone Linkage on the pH Stability of PEG - PE Conjugates,” pp. 363–370, 2007.

[78] W. Fan, X. Tong, Q. Yan, S. Fu, and Y. Zhao, “Photodegradable and size-tunable single-chain nanoparticles prepared from a single main-chain coumarin-containing polymer precursor,” *Chem. Commun.*, vol. 50, pp. 13492–13494, 2014, doi: 10.1039/C4CC06629D.

[79] Q. Jin, Y. Wang, T. Cai, H. Wang, and J. Ji, “Bioinspired photo-degradable amphiphilic hyperbranched poly (amino ester) s : Facile synthesis and intracellular drug delivery,” *Polymer (Guildf).*, vol. 55, no. 18, pp. 4641–4650, 2014, doi:

10.1016/j.polymer.2014.07.053.

[80] J. F. Folmer-andersen and J. Lehn, “Thermoresponsive Dynamers : Thermally Induced , Reversible Chain Elongation of Amphiphilic Poly (acylhydrazones),” pp. 10966–10973, 2011.

[81] M. Khan, “美国科学院学报 Materials Chemistry A 材料化学 a,” *J. Mater. Chem. A*, no. 207890, p. 121, 2015, doi: 10.1039/D0TA01419B.Volume.

[82] M. A. Theodoropoulou, N. F. Nikitas, and C. G. Kokotos, “Aldehydes as powerful initiators for photochemical transformations,” *Beilstein J. Org. Chem.*, vol. 16, pp. 833–857, 2020, doi: 10.3762/bjoc.16.76.

[83] Q. Zhou, L. Zhang, T. H. Yang, and H. Wu, “Stimuli-responsive polymeric micelles for drug delivery and cancer therapy,” *Int. J. Nanomedicine*, vol. 13, pp. 2921–2942, 2018, doi: 10.2147/IJN.S158696.

[84] F. Xu, H. Li, Y. L. Luo, and W. Tang, “Redox-Responsive Self-Assembly Micelles from Poly(N-acryloylmorpholine-block-2-acryloyloxyethyl ferrocenecarboxylate) Amphiphilic Block Copolymers as Drug Release Carriers,” *ACS Appl. Mater. Interfaces*, vol. 9, no. 6, pp. 5181–5192, 2017, doi: 10.1021/acsami.6b16017.

[85] A. Lu *et al.*, “Self-assembled micelles prepared from bio-based hydroxypropyl methyl cellulose and polylactide amphiphilic block copolymers for anti-tumor drug release,” *Int. J. Biol. Macromol.*, vol. 154, pp. 39–47, 2020, doi: 10.1016/j.ijbiomac.2020.03.094.

[86] F. Y. Qiu, M. Zhang, R. Ji, F. S. Du, and Z. C. Li, “Oxidation-Responsive Polymer-Drug Conjugates with a Phenylboronic Ester Linker,” *Macromol. Rapid Commun.*, vol. 36, no. 22, pp. 2012–2018, 2015, doi: 10.1002/marc.201500349.

[87] X. Guo, C. Shi, J. Wang, S. Di, and S. Zhou, “PH-triggered intracellular release from actively targeting polymer micelles,” *Biomaterials*, vol. 34, no. 18, pp. 4544–4554, 2013, doi: 10.1016/j.biomaterials.2013.02.071.

[88] J. Du, X. Du, C. Mao, and J. Wang, “Tailor-Made Dual pH-Sensitive Polymer À Doxorubicin Nanoparticles,” pp. 17560–17563, 2011.

[89] “Journal of Liquid Chromatography & Related Technologies Handbook of Instrumental Techniques for Analytical Chemistry,” no. December 2014, pp. 37–41, 2006, doi: 10.1080/10826079808006889.

[90] S. H. Crouch, *Instrumental Analysis Principles*. 2018.

[91] M. S. Braga *et al.*, “Multispectral colorimetric portable system for detecting metal ions in liquid media,” *2019 4th Int. Symp. Instrum. Syst. Circuits Transducers*, no. August, pp. 1–6, 2019, doi: 10.1109/INSCIT.2019.8868861.

[92] Light Scattering from Polymer Solutions and Nanoparticle Dispersions, Wolfgang Schärtl, Springer Laboratory,

[93] S. Bhattacharjee, “Review article DLS and zeta potential – What they are and what they are not ?,” *J. Control. Release*, vol. 235, pp. 337–351, 2016, doi: 10.1016/j.jconrel.2016.06.017.

[94] S. B. Methods, “2 Scanning Beam Methods.”

[95] D. B. Williams and C. B. Carter, “M icroscopy M icroanalysis Transmission Electron Microscopy — A Textbook for Materials Science,” no. Chapter 1, pp. 452–453, 1999.

[96] A. Bose, I. Thomas, G. Kavitha, E. Abraham, and A. Bose, “International Journal of Advances in Pharmaceutical Analysis Fluorescence spectroscopy and its applications : A Review * Article History :,” vol. 08, no. 01, pp. 1–8, 2018.

Appendix 1

Characterization Techniques

1. Size Exclusion Chromatography

Size exclusion chromatography (SEC), also known as gel permeation chromatography (GPC), is a polymer separation method which allows the determination of the polymer molecular weight and molecular weight distribution [55, 56]. Porath and Flodin [57] were the first to report that polymers can be separated based on their size via their penetration through a packed porous material. The term gel permeation chromatography was defined by Moore [58], who developed rigid cross-linked polystyrene gels with a range of pore sizes, suitable for separation of synthetic polymers in organic media. SEC is extremely valuable for both analytic and preparative work with a wide variety of systems ranging from low to very high polymer molecular weights. The method can be also applied to a wide variety of solvents and polymers, depending on the type of gel used. A SEC instrument usually involves a pump, a detector (e.g. UV or RI or both) and one, two or more separating columns (**Figure 1A**). The pump circulates the solvent through the series of columns filled with porous beads (**Figure 1B**). Often the beads are solvent swollen polymer gel particles. The beads are intentionally made with a variety of pores sizes that span the range of the sizes of the macromolecules to be separated. A small volume of a dilute polymer solution in the same solvent is injected into the flowing solvent stream entering the columns. As the polymer solution passes thought the columns, the largest polymers are excluded from all but the largest pores, and elute from the column first. Progressively, smaller polymers can explore the smaller pores and therefore, larger volumes of the column and consequently elute later (**Figure 1C**). Thus, the separation of molecules in SEC occurs by polymer size rather than polymer mass. After separation, the solution passes through the detectors that are used in the system and are analyzed upon proper calibration with narrow molar mass distribution standards.

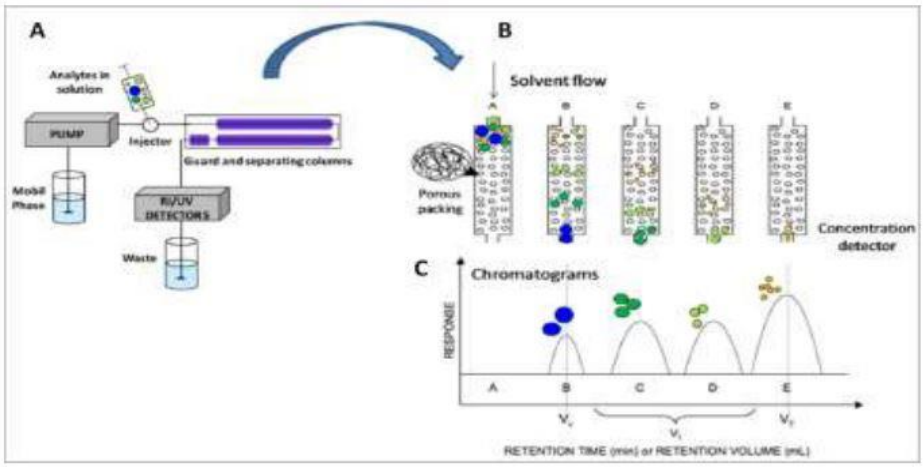

Figure 1. Schematic illustration of the SEC instrument. A) Main parts of a SEC, B) separation columns and C) representative retention time of a polymer depending on its size.

2. ^{1}H Nuclear Magnetic Resonance spectroscopy (^{1}H NMR)

Nuclear magnetic resonance spectroscopy is a very useful and commonly used technique for determining the chemical structure of compounds [89]. ^{1}H NMR and ^{13}C NMR are the most widely used material characterization methods. Nuclear magnetic resonance is a spectroscopic technique used to observe the local magnetic field around the nucleus. The sample containing the material is placed in a magnetic field and the core of the sample is excited in nuclear magnetic resonance through radio waves, thus generating a nuclear magnetic resonance signal, which is detected by a sensitive radio receiver (**Figure 2**). Different nuclei absorb electromagnetic radiation of different wavelengths depending on the chemical and electronic environment. The location and pattern of the NMR signal provide the necessary information about the nuclear environment. The exact field strength of the core (in ppm) resonates with the reference standard, usually the signal from the deuterated solvent used. The electron cloud protects the nuclei from external magnetic fields, causing them to absorb at a higher energy (lower ppm), while adjacent functional groups "deshield" the nuclei, causing them to absorb at a lower energy (higher ppm). Chemically and magnetically equivalent nuclei resonate with the same energy and give a single signal or mode. Protons on adjacent carbon atoms interact and split the resonance into multiple peaks, following the n + 1 rule, and the coupling constant is J. Spin coupling is usually observed between nuclei separated by 1, 2 and 3 bonds. The area under the NMR resonance is proportional to the number

of nuclei generating the resonance, so the proton of the resonance can be calculated by integration.

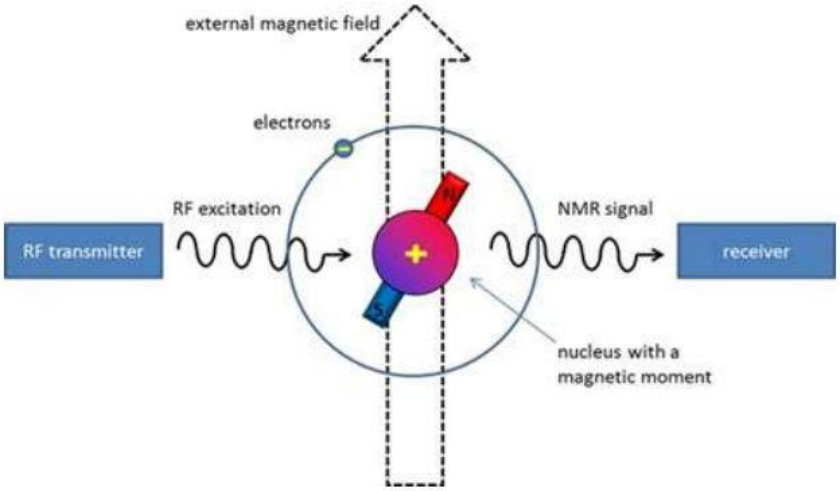

Figure 2. NMR phenomenon.

3. Attenuated Total Reflectance –Fourier Transform Infrared (ATR-FTIR) spectroscopy

Infrared spectroscopy (IR) is considered an important spectroscopic technique because of the ease of obtaining spectra and comparing them with spectra of known compounds. It is widely used in the synthesis of chemical compounds and for certifying their purity. In order to draw conclusions about the concentration of a component in a sample (taking into account that the amount of energy absorbed is a function of the number of molecules present), the depth of a characteristic absorption band is compared with the depth of the same band of a spectrum containing a known concentration of that component.

The absorption of infrared radiation is limited to molecules which exhibit small energy differences between different vibrational and rotational energy states. In order to absorb infrared radiation, a molecule must undergo a change in its dipole moment as a result of its vibrational or rotational motion, as is the case with heteronuclear molecules. Thus, each molecule gives its own characteristic absorption spectrum, which can be considered as the 'fingerprint' of the molecule. When homonuclear, diatomic molecules such as O_2, N_2, Cl_2 vibrate or rotate, there is no net change in their dipole moment. Consequently, such molecules do not absorb in the infrared region of the spectrum. The infrared radiation is absorbed by a molecule at frequencies below 100 cm-1 and is converted into molecular bond rotation energy. Similarly, infrared radiation absorbed by a molecule between 10000 - 100 cm^{-1} is converted into vibrational bond energy.

The frequency or wavelength of an absorption depends on the relative masses of the atoms, the bond strength constants and the geometry of the atoms. The different positions in the IR spectrum are designated as wavelength units, the unit of which is cm^{-1} (wavenumber).

There are two types of molecular vibrations: tension vibration and bending vibration (**Figure 3.1**). Tension vibration involves rhythmic movement along the axis of the bond so that the distance between atoms increases or decreases in the form of an oscillation. During bending vibration, there is either a change in the angle of two bonds with a common atom, or movement of a group of atoms relative to the rest of the molecule provided that the atoms of the moving group remain stationary relative to each other.

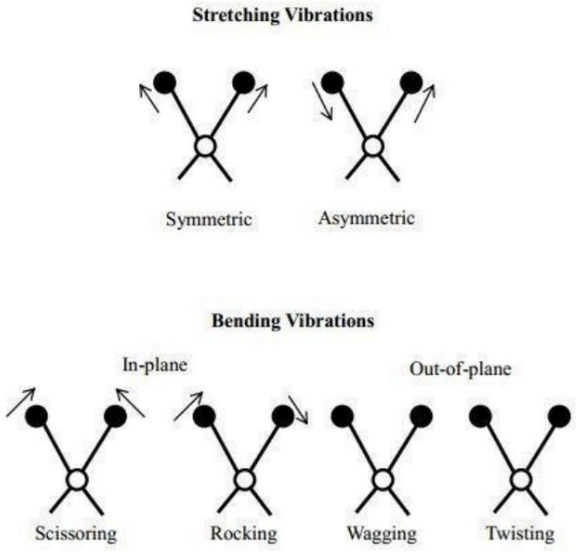

Figure 3.1. Types of molecular vibrations.

The application area of infrared spectroscopy has been greatly expanded in the last decades due to the development of Fourier transform infrared spectroscopy. In standard infrared spectroscopy, the multichromatic radiation from the source is analyzed using a monochromator (prism or barrier) and detected at frequencies n + Δv, where Δv is determined by the slit width of the photometer. In Fourier transform infrared spectroscopy, a key part of the technique is the Michelson interferometer, known since the end of the 19th century. According to the principle of Michelson interferometers, the radiation initially arrives in a beamsplitter and the two individual beams contribute after being reflected in a mirror. The intensity of the radiation is measured as a function of the displacement of the mirror. The interferograms obtained give information on the total absorption of the sample by wavelength and intensity as the Fourier sum of all spectral lines.

The method used in these experiments is the attenuated total reflection (ATR) technique which has many advantages. In this method the IR beam is directed through an internal reflection element (a crystal - usually a diamond) of high refractive index (**Figure 3.2**). The IR light is totally internally reflected by the back surface, which is in contact with the sample mounted on a Zn - Se (zinc - selenium) crystal. Upon reflection at the crystal - sample interface, the IR radiation penetrates the sample and thus IR data are obtained from the sample. The main advantage of this technique is the easy preparation of the sample to be studied.[90]

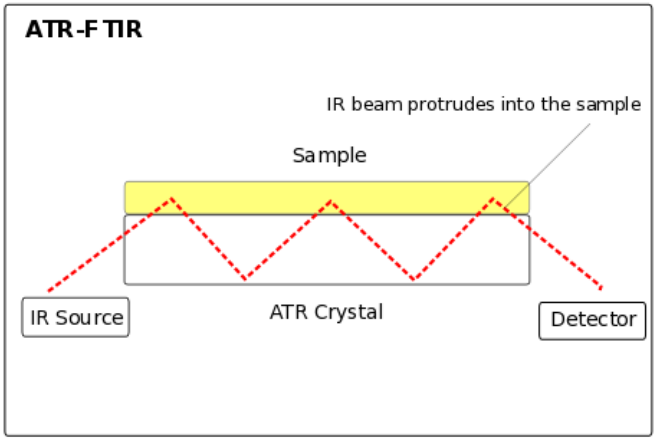

Figure 3.2. Light undergoes multiple internal reflections in the crystal of high refractive index, shown in white. The sample is in contact with the crystal.

4. UV-VIS spectroscopy

UV/Vis spectroscopy is a regularly used technique for the characterization of both organic and inorganic materials [90]. The range of wavelengths that correspond to the UV/Vis spectrum is from 200 to 800 nm, from which 200-400 nm is the ultraviolet region and 400-800 nm is the visible region. When molecules that comprise π-electrons are irradiated with UV/Vis light they absorb this energy and electronic transitions take place. The absorbance A can be described by the Beer-Lambert law that correlates the absorption with the concentration of the absorbing species as shown in the following equation:

$$A=\log 10\ (I_0/I) = \varepsilon * L * c$$

Where (I_0) is the intensity of the incident light, (I) is the intensity of the transmitted light, (ε) is the absorption coefficient, which is constant for a specific substance and depends on the wavelength, the solvent and the temperature, (L) is the path length through the sample and (c) the concentration of the sample.

A typical double beam UV/Vis spectrometer is shown in **Figure 4**. There are five basic components in a simple double beam UV/Vis spectrophotometer; a light source, a monochromator, a sample compartment, a beam splitter and a detector. The monochromator of the instrument is composed of an entrance slit (to narrow the beam to a usable size), a dispersion device (usually a diffraction grating or prism that separates polychromatic white light into bands of monochromatic light of a single wavelength), and an exit slit (to select the desired monochromatic wavelength). In a typical experiment a beam of light from the light source is separated into its component wavelengths by a prism or diffraction grating. Each monochromatic beam in turn is split into two equal intensity beams by a beam splitter. One beam, the sample beam, passes through a small cuvette containing a solution of the compound being studied in a transparent solvent. The other beam, passes through an identical cuvette containing only the solvent. The intensities of these light beams are then measured by electronic detectors and compared. The intensity of the reference beam, which should have suffered little or no light absorption, is defined as I_0. The intensity of the sample beam is defined as I. Over a short period of time, the spectrometer automatically scans all the component wavelengths.

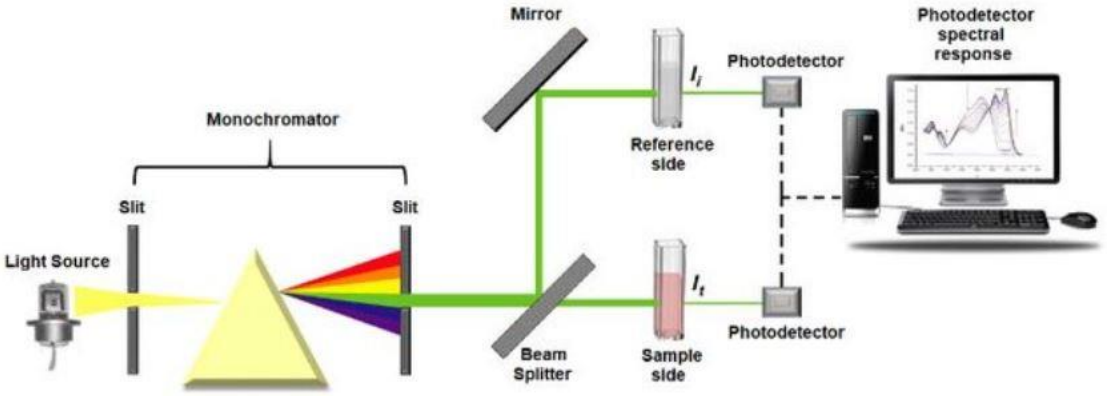

Figure 4. Schematic representation of a double beam UV-VIS spectrophotometer [91].

5. Dynamic Light Scattering (DLS)

Dynamic light scattering, also known as photon correlation spectroscopy (PCS) or quasi-elastic light scattering (QLS), is a spectroscopic method, mainly used to determine the size distribution of particles (polymers, colloids, nanoparticles etc.) in solution or suspension [92]. What DLS measures, is the Brownian motion of the particles in the solution due to the constant collisions between them and the molecules of the solvent, and it relates that motion to the size of the particles. Generally, the larger the particle, the slower the Brownian motion, while smaller particles are further displaced after the collision with the solvent molecules and so move more rapidly. The velocity of the Brownian motion in each case is expressed by the translational diffusion coefficient, D. The translational diffusion coefficient is part of the Stokes-Einstein equation that calculates the size of the particle as follows:

$$d\,(H) = kT\ 3\pi\eta D$$

Where d(H) is the hydrodynamic diameter of the particle, D is the translational diffusion coefficient, k is Boltzmann's constant, T is the absolute temperature and η is the viscosity. The diameter that is calculated by this function is the diameter of a sphere that is characterized by the same translational diffusion coefficient as the particle being measured. The translational diffusion coefficient depends on a number of factors: i) the size of the "core" of the particle, ii) the ionic strength of the medium (low conductivity media generate an extended layer of ions around the particle, thus reducing the diffusion speed and lead to an apparently larger hydrodynamic diameter) and iii) the surface structure (any change in the surface of the particles that can have an effect on the speed of the particles' diffusion, will lead to a corresponding change in the apparent hydrodynamic size of the particles).

When the particles that are going to be measured are small compared to the laser that is used during the measurement (typically around λ /10), the scattering from the particles is of the same energy as the incident light (elastic scattering) and is not angle dependent (Rayleigh scattering) [93]. When the size of the particles exceeds that threshold though, Rayleigh scattering is replaced by Mie scattering, that is anisotropic, so the scattered light is of unequal energy in relation to the incident light (inelastic scattering) as well as angle dependent (the scattered light is more intense in the direction of the incident light, and bigger particles exhibit higher angle-dependence). During a dynamic light scattering measurement, the speed of the diffusing, due to Brownian motion, particles is measured. The measurement is essentially the rate at which the intensity of the scattering light fluctuates and is detected by a suitable detector. This measurement is reflected

by a speckle pattern, in which the position of each speckle constantly changes, since the system is in constant Brownian motion. The rate at which the intensity fluctuates depends on the size of the particles, for example small particles lead to more fluctuations in the measured intensity. The frequencies of the intensity fluctuations are recorded by a digital autocorrelator. An autocorrelator is essentially a signal comparator that, in the case of DLS, compares one signal with itself at various time intervals. By comparing the intensity of the signal at time equal to t to the intensity of the signal at a very short time after that (t+δt), the relationship between the two signals, or else their correlation, will be very strong. The same process is repeated for longer amounts of time and it is noted that the correlation reduces with time. The correlation is also dependent on the size of the particles, as large particles do not exhibit quick changes in their intensity fluctuations, so the correlation can persist for a longer amount of time in comparison to smaller particles that move rapidly and cause high fluctuations in their intensity, so their correlation exhibits a quicker reduction. The correlation function of the scattered intensity created by the correlator is the following:

$$G(\tau) = < I(t)I(t + \tau) >$$

Where τ is the time difference of the correlator.

When the correlation function refers to a large number of monodisperse particles that are in Brownian motion, it is an exponential decaying function of the correlator time delay τ:

$$(\tau) = [1 + B \exp(-2\Gamma\tau)]$$

Where A is the baseline of the correlation function and B the intercept of the correlation function. Γ is given by the equation $\Gamma = Dq^2$. D is the translational diffusion coefficient, and the wavevector q is expressed as $q = 4\pi\ (n\ /\lambda_0)\sin(\theta/\ 2)$, where n is the refractive index of the dispersant, λ is the wavelength of the laser and θ is the scattering angle.

In the correlogram that derives from a measurement, the time at which the correlation starts to decay in a significant amount gives an indication of the mean size of the particles in the sample. More monodisperse samples generate steeper decaying, while more polydisperse samples lead to extended decay times. The size can be obtained from the correlation function with the use of various algorithms. The size distribution that derives from them is a plot of the relative intensity of the scattered light by the various sized particles in the sample and is known as the intensity size distribution. If it is a single smooth peak, there is no need for converting it to a volume distribution

using the Mie theory. A typical DLS instrument consists of three components: the laser, the sample and the light detector.

6. Scanning Electron Microscopy (SEM)

Scanning electron microscopy allows the depiction of high-resolution and high-magnification images of a sample, which is placed on an appropriate surface. A tungsten filament emits electrons, which are focused by an electron optical system. The electron beam produced is capable of scanning the sample surface and provide the composition at a point, along a line or over a rectangular area, by moving the beam across the surface in a series of parallel lines. Movement along the three directions, x, y and z is possible, as the sample is placed over a stage that moves depending on the desire of the user. SEM can be utilized to visualize almost any type of sample. The instrument operates in high vacuum and very dry environment in order to produce the high energy beam of electrons needed for imaging. The imaging system depends on the electrical conductivity of the specimen to ensure that the bulk of the incoming electrons go to ground. Therefore, the samples are coated with conductive materials, Au being the most common. As the high electron beam interacts with the sample, different signals are scattered. Collection of these enables the formation of the image. Two principal signals are used to form images, backscattered electrons and secondary electrons that are generated within the primary beam-sample interactive volume. The backscattered electron coefficient increases with increasing the specimen's atomic number, whereas the secondary electron coefficient is relatively insensitive to atomic number. This difference plays an important role in the way the samples may need to be prepared. The use of scanning electron microscopy may be considered when the user is able to interpret the information obtained from SEM and attempt to relate the form and structure of the two-dimensional images and identity of the chemical data back to the three-dimensional sample from which the information was derived [94]. A typical SEM setup is presented below.

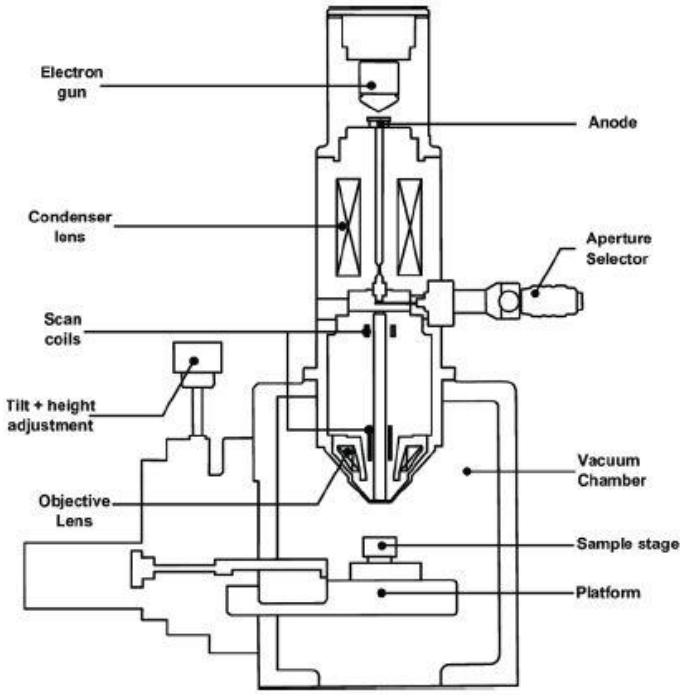

Figure 6. Schematic representation of a SEM setup.

7. Transmission Electron Microscopy (TEM)

Transmission electron microscopes (TEM) are microscopes that use a particle beam of electrons to visualize specimens and generate a highly-magnified image [95]. TEMs can magnify objects up to 2 million times. TEMs employ a high voltage electron beam in order to create an image. An electron gun at the top of a TEM emits electrons that travel through the microscope's vacuum tube. Rather than having a glass lens focusing the light (as in the case of light microscopes), the TEM employs an electromagnetic lens which focuses the electrons into a very fine beam. This beam then passes through the specimen, which is very thin, and the electrons either scatter or hit a fluorescent screen at the bottom of the microscope. An image of the specimen with its assorted parts shown in different shades according to its density appears on the screen. This image can be then studied directly within the TEM or photographed. **Figure 7** shows a diagram of a TEM and its basic parts.

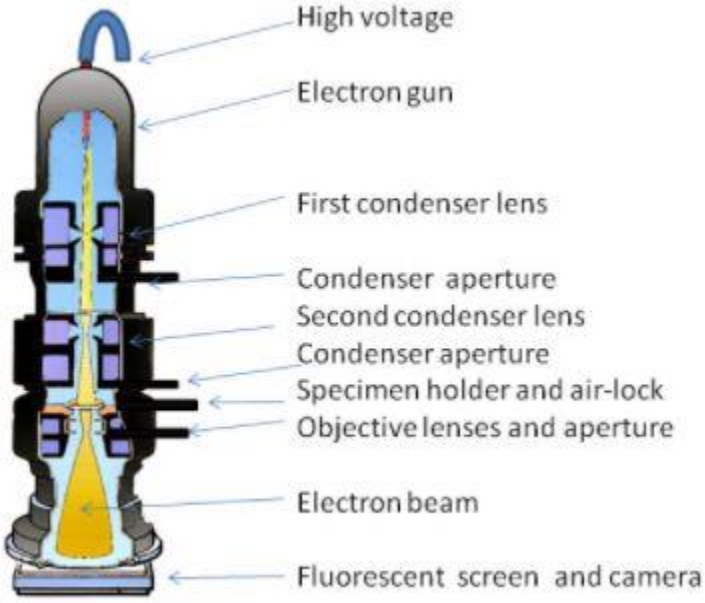

Figure 7. Schematic representation of TEM.

8. Fluorescence Spectroscopy

Fluorescence is the phenomenon in which a molecule absorbs light within its absorption band and then emits this light at longer wavelengths within its emission band. This phenomenon can be used to identify, quantify, and observe chemical activity, and it is a popular method due to its high level of sensitivity, simplicity, and specificity.

Fluorescence spectroscopy is a spectroscopy method used to analyze the fluorescence properties of a sample by determining the concentration of an analyte in a sample. This technique is widely used for measuring compounds in a solution, and it is a relatively easy method to perform.

Fluorophores play the central role in fluorescence spectroscopy. Fluorophores are the components in molecules that cause them to fluorescence. Fluorophores typically contain several combined aromatic groups, or planar or cyclic molecules with several π bonds. Absorption of UV or visible radiation causes transition of electrons from the singlet ground state to the singlet excited state. As this state is not stable, it emits energy in the form of UV or visible radiation and returns to the singlet ground state. Fluorescence emission occurs as the fluorophore decays from the singlet electronic excited states to an allowable vibrational level in the electronic ground state (**Figure 8.1**). The fluorescence excitation and emission spectra reflect the vibrational level structures in the ground and the excited electronic states, respectively.[96]

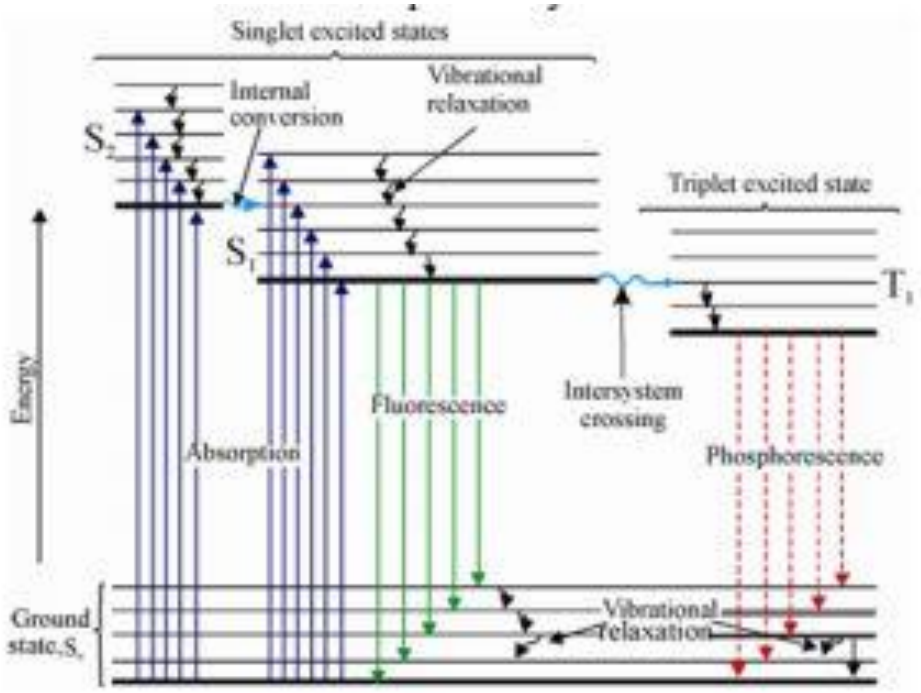

Figure 8.1. Jablonski diagram illustrating different transitions between a molecule's energy states.

A spectrofluorometer (**Figure 8.2**) mainly consists of:

A. Source of light: Mercury vapour lamp, Xenon arc lamp, Tungsten film

B. Filters and monochromators: Primary filters and secondary filters, Excitation monochromators and Emission monochromators

C. Sample cells, Detectors

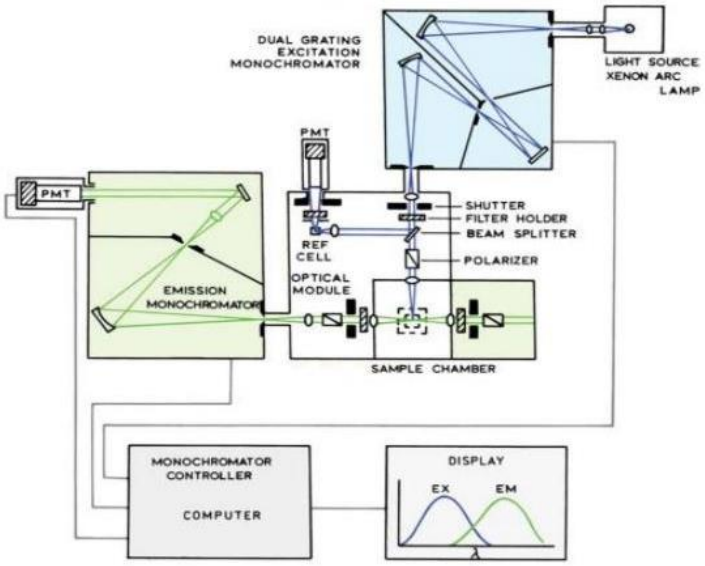

Figure 8.2. Schematic diagram of a spectrofluorometer.